Utah State University

DigitalCommons@USU

All Graduate Theses and Dissertations, Fall 2023 to Present

Graduate Studies

8-2024

Trade-Offs in Lighting for DIC Strain Measurements in Vibration-Based Fatigue Testing

Jacob R. Rigby
Utah State University

Follow this and additional works at: https://digitalcommons.usu.edu/etd2023

 Part of the Aerospace Engineering Commons, and the Mechanical Engineering Commons

Recommended Citation

Rigby, Jacob R., "Trade-Offs in Lighting for DIC Strain Measurements in Vibration-Based Fatigue Testing" (2024). *All Graduate Theses and Dissertations, Fall 2023 to Present*. 308.
https://digitalcommons.usu.edu/etd2023/308

This Thesis is brought to you for free and open access by the Graduate Studies at DigitalCommons@USU. It has been accepted for inclusion in All Graduate Theses and Dissertations, Fall 2023 to Present by an authorized administrator of DigitalCommons@USU. For more information, please contact digitalcommons@usu.edu.

TRADE-OFFS IN LIGHTING FOR DIC STRAIN MEASUREMENTS IN VIBRATION-BASED FATIGUE TESTING

by

Jacob R. Rigby

A thesis submitted in partial fulfillment
of the requirements for the degree

of

MASTER OF SCIENCE

in

Mechanical Engineering

Approved:

_____	_____
Ryan B. Berke, Ph.D. Major professor	Thomas H. Fronk, Ph.D. Committee member
_____	_____
Barton L. Smith, Ph.D. Committee member	D. Richard Cutler, Ph.D. Vice Provost of Graduate Studies

UTAH STATE UNIVERSITY
Logan, Utah

2024

Copyright © Jacob Rigby 2024

All Rights Reserved

ABSTRACT

Trade-offs in Lighting for DIC Strain Measurements in Vibration-based Fatigue Testing

by

Jacob Rigby, Master of Science

Utah State University, 2024

Major Professor: Dr. Ryan B. Berke
Department: Mechanical Engineering

Digital Image Correlation (DIC) is a popular camera-based, non-contacting method to obtain full-field displacement and strain measurements. In a vibration-based fatigue test, DIC is desirable because DIC can continue to monitor strain in the specimen after a strain gage would have failed. One of the major challenges of DIC is maintaining sufficient lighting on a test specimen throughout a vibration test. Large out-of-plane displacements necessitate small apertures for improved depth of field while high frequency testing requires short exposure times to reduce motion blur. In this work, the trade-offs in aperture, exposure time, gain, and external lighting (ring lights and strobe lights) are examined to compare the different external lighting sources and determine if gain can be utilized without negatively impacting the strain measurement. First, a Design of Experiment (DOE) response surface test matrix is generated for each external lighting condition and aperture size. Second, derivatives were taken on a Euler-Bernoulli fit solution to the out of plane displacement (W) data obtained from DIC to obtain strain data. Third, the derived strain was compared to the extrapolated strain from displacement measurements to create a baseline for comparison. Further, a Monte Carlo Method uncertainty propagation was

performed to determine the uncertainty between the two strain measurements. The strobe lights provided the most accurate and stable strain measurements while the ring lights provided the smallest tolerance range. Increasing the gain level typically had no impact on the strain measurement or the uncertainty except in the cases of extremely small apertures. In this case, gain proved to be beneficial to increase the accuracy and decrease the uncertainty range of the analytical solution.

(74 Pages)

PUBLIC ABSTRACT

Trade-offs in Lighting for DIC Strain Measurements in Vibration-based Fatigue Testing

Jacob Rigby

Vibration based fatigue testing offers a fast and efficient method for determining the breaking point of a material. This method often uses a device, called a strain gage, to measure the deformation of a test sample at a single spot on the test sample. However, these strain gages often break before testing is complete. To overcome this premature break, a laser vibrometer is often used to measure the amount of movement or the speed of the test sample throughout the vibration test. The deformation measured by the strain gage is compared against the amount of movement or velocity of the test specimen as measured by the laser vibrometer to allow for future comparison after the strain gage breaks. As an alternative to strain gages, Digital Image Correlation (DIC) is a popular camera-based, non-contacting method that determines the movement and deformation across the entire test sample. In a vibration-based fatigue test, DIC is desirable because DIC can continue to monitor the deformation in the test sample even after a strain gage would have broken. However, one of the major challenges of DIC is maintaining sufficient lighting on a test sample throughout a vibration test. Large motions towards the cameras require small apertures for improved depth of field while fast moving test samples require short exposure times to reduce motion blur. In this work, the trade-offs between aperture, exposure time, gain (artificial brightness), and external lighting (ring lights and strobe lights) is examined to compare the different lighting sources and determine if artificially increasing the

brightness of an image by using gain can successfully be used without negatively impacting the deformation measurement from DIC. This was accomplished by first creating a series of tests that vary the aperture, exposure time, and gain for two different light sources. Second, an analytical solution was applied to the DIC movement measurements to allow for calculation of the strain on the test sample. Third, the deformation was compared to the calculated deformation from the movement measured by the laser vibrometer to provide a common comparison point between the different lighting tests. The tests performed showed the strobe lights provided the most stable and accurate results, but the ring lights had the lowest amount of difference between measurements. Artificially brightening the image through gain typically had no impact on the calculated deformation or the variation between measurements, except in the case of extremely small apertures. In this case, artificial brightening proved to be beneficial to increase the accuracy and decrease the variation of the analytical solution.

ACKNOWLEDGMENTS

First, I would like to express my gratitude to my advisor, Dr. Ryan Berke, for his mentorship, patience, and guidance throughout my academic career. He has always been supportive in working with me while I have attempted to balance school life, work life, and family life. I would also like to thank my fellow co-researchers from the Mechanics at Extreme Temperatures Lab who have helped contribute to this work. Many of the analysis techniques used in this work would not have been possible without their dedication and expertise.

I would also like to express my deepest gratitude to my wife, son, daughter, and other family members and friends for supporting me during my weekend trips to the lab and late nights analyzing data. They have encouraged and motivated me to continue when issues arose. I would not have been able to complete this work without them.

Jacob R. Rigby

CONTENTS

Page

LIST OF TABLES

Page

LIST OF FIGURES

Page

CHAPTER 1

INTRODUCTION

1.1 Vibration-based Fatigue Testing

Certain structural components, such as those found in wind turbines [1], gas turbines [2], nuclear power applications [3], and aerospace structures [4], experience high cycle fatigue (HCF) through their service time. Design tools like stress versus cycles to failure (S-N) curves are commonly utilized to design these structural components to withstand HCF [5]. Conventional axial testing methods can take up to 70 hours to collect a single data point for the S-N curve due to the low frequency (~40 Hz) of a standard servo-hydraulic test machine [6]. Vibration-based fatigue testing has the advantage over conventional testing by generating uniaxial bending stress data under fully reversible bending [7] at a much faster rate (up to 50 times faster) by using higher frequency resonant modes (1200-2000Hz) [8].

In 2004, George et al. developed a novel vibration-based fatigue test in which a base excitation is applied to a cantilevered square plate specimen using an electrodynamic shaker. The specimen is then excited to the chord-wise bending mode, also known as the "two-stripe" mode, named for the two nodal lines running the length of the specimen [7]. The two-stripe mode creates fully reversible, uniaxial bending in the center of the free edge of the plate, as shown in Figure 1. This location is commonly called the "fatigue zone" and is where failure is predicted to occur [9]. Compared to other vibration modes, some benefits of this mode include: (1) the stress in the fatigue zone is significantly higher than anywhere

else in the plate, which ensures that fatigue failure occurs at a predictable location at which sensors can be directed, while avoiding other interaction effects such as fretting at the clamped edge; and (2) the frequency of the mode is sufficiently isolated from other neighboring modes such that they do not influence the mode shape. In 2021, Furman et al. performed a shape optimization analysis and determined that in addition to square plates, rectangular plates with a length-to-width ratio of 1.37 also meet these criteria and are thus suitable for fatigue testing under the two-stripe mode [10].

Figure 1

FEA Simulation of the (a) Out-of-Plane Displacement and (b) von-Mises Strain of the Two-Stripe Mode for a Cantilevered Rectangular Plate [11]

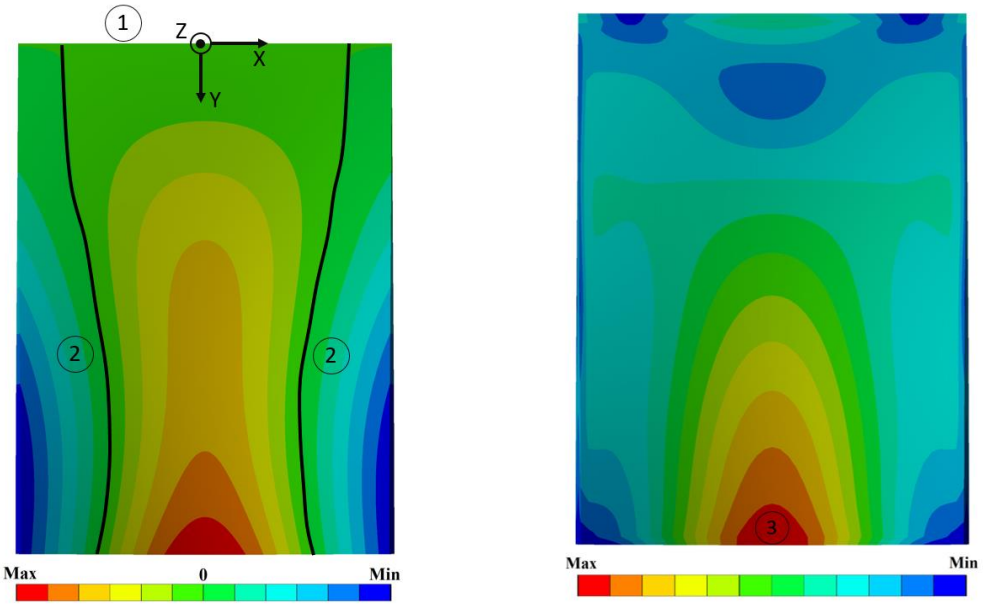

(a) (b)

1 – Clamped Edge 2 – Nodal Lines (Drawn for Emphasis) 3 – Fatigue Zone

In 2015, Bruns, Zearley et al.[1] developed a carrier-insert plate assembly consisting of a reusable carrier plate and an expendable insert specimen to reduce waste during vibration fatigue testing [8]. In 2017, Scott-Emuakpor et al. improved the carrier-insert system design by tapering the gauge section of the insert specimen to be consistent with the ASTM bending fatigue standard, thereby minimizing damage accumulation on the carrier plate, reducing system damping, and improving the repeatability of the experimental response [12]. Figure 2 depicts the two-stripe bending mode on the improved carrier-insert design.

Figure 2

FEA Simulation of the (a) Out-of-plane Displacement and (b) von-Mises Strain of the Two-Stripe Mode on the Improved Carrier-Insert Plate Design

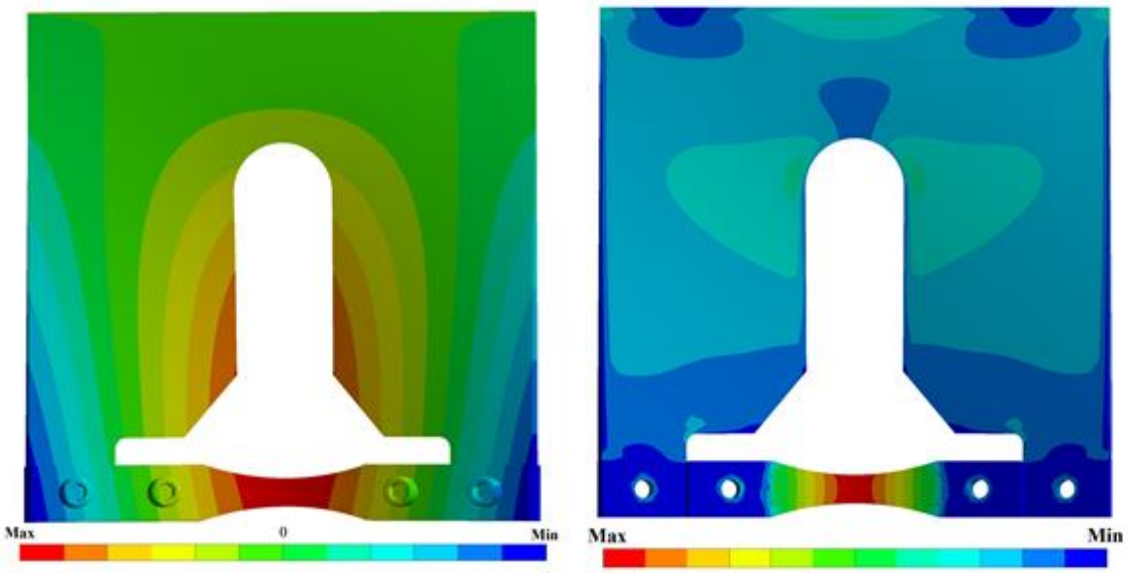

(a) (b)

[1] Jeff Bruns and Alyssa Zearley are credited in the paper as co-first authors. In recognition of this status, this thesis will credit both authors as appropriate.

Throughout the duration of fatigue life experiments, the strain must be monitored until failure of the specimen [13]. The vibration-based test performed by George et al. and Bruns-Zearley et al. originally placed a strain gauge in the fatigue zone of the plate [7] or the insert specimen [8] to monitor strain during the vibration test. However, strain gauges have their own fatigue limit and often fail before the specimen [13]. Additionally, strain gauges require considerable time and labor to apply [14]. To overcome the fatigue life of the strain gage, the method performed by George et al. used a non-contacting laser vibrometer that had the velocity reading calibrated against the strain gage to maintain a consistent strain level beyond the life of the strain gage [7], as shown in Figure 3. However, this approach assumes that velocity (as measured by the vibrometer) and strain (as would have been measured by a strain gage) remain linearly proportional after the strain gage has failed, even as the specimen accumulates damage in the form of fatigue crack growth. Non-contacting strain measurement techniques, such as Digital Image Correlation (DIC), overcome many of the limitations of strain gauges because DIC continues to monitor strain in the specimen after the strain gage would have failed.

Figure 3

Example of Strain-Velocity Calibration Curve taken from [7]

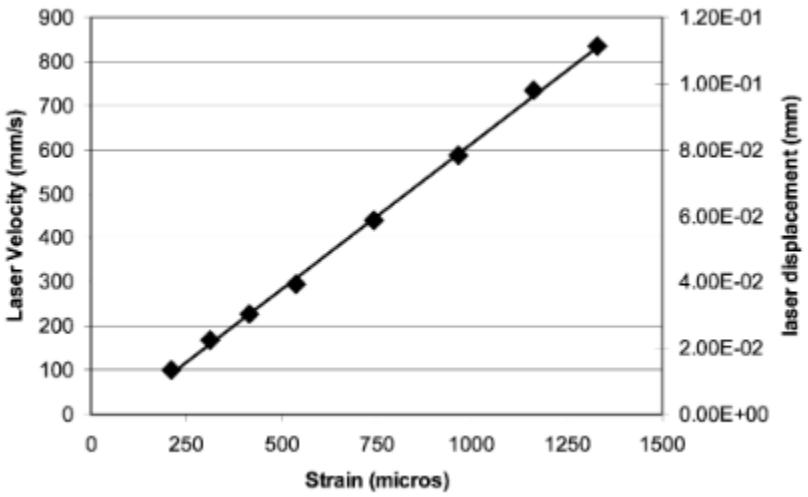

In 2022, Hill et al. developed a procedure to reduce the dependence on strain gauges during vibration fatigue tests by applying a family of curve fitted equations derived from plate theory to the displacements and strains obtained using DIC along the free edge of a rectangular plate. The strains derived from this novel procedure matched the strain gauge readings at the edge of the rectangular plate to within 1% at fatigue level strains [11]. However, the analytical solution developed by Hill et al is specific to square [7] and rectangular [10] plates, not the carrier-insert assemblies developed by Bruns, Zearley et al [8]. The enclosed work builds directly on Hill's work by extending his methodology to a Bruns-Zearley style carrier-insert assembly, while further exploring the role that lighting plays in the quality of the resulting measurements.

1.2 Digital Image Correlation

DIC is a popular non-contacting method to obtain full-field displacement and strain measurements [15]. The technique works by applying a high-contrast pattern to the surface of a deformable specimen, and using high-resolution cameras to track the motion of that pattern [16]. When performed using a single camera, the technique is limited to 2D measurements (also known as 2D-DIC or planar DIC) at a fixed distance away from the camera [15]. By using two or more cameras (also known as 3D-DIC or stereo DIC), the cameras can triangulate the position of the specimen's surface to capture out of plane displacements [17].

The DIC algorithm partitions a user specified region of interest into subsets of pixels, the width of which is often called the subset size (SS). The distance between the center of overlapping subsets is often called the step size (ST) [18]. The displacement of the pixel subsets is calculated using an image correlation algorithm to minimize some version of the sum of squared differences (SSD) criterion, shown in Equation 1.1 [19].

$$c(x,y,u,v) = \sum_i \sum_j \left(I(x+i,y+j) - I^*(x+u+i,y+v+j)\right)^2 \qquad (1.1)$$

Where:

$c(x,y,u,v)$ = correlation function

x, y = pixel coordinates

u, v = displacements

$i = i^{th}$ x-coordinate in subset

$j = j^{th}$ y-coordinate in subset

I = Intensity before motion

I^* = Intensity after motion

More advanced DIC algorithms use normalized sum of squared differences (NSSD) or zero-normalized sum of squared differences (ZNSSD) correlation functions. These functions reduce error in the correlation function by accounting for linear scaling in lighting and uniform offsets in lighting [20]. The correlation function can be further improved by using sub-pixel interpolation, a subset shape function that allows future subsets to deform, and higher order Taylor Expansions [21].

Once the correlation function identifies the location of the subsets in the deformed image, the DIC algorithm can calculate the relative full-field displacements between the undeformed image (also known as a reference image) and deformed image. While DIC is fundamentally measures displacement, the strains are frequently calculated as the derivatives of the displacement [18]. However, numeric differentiation of the displacements often introduces a significant amount of noise into the strain measurement. To reduce the noise, the strain measurement is averaged over a number of subsets, called the strain window (SW) or filter size. The relationship between the subset size, step size, and strain window is illustrated in Figure 4.

Figure 4

Interaction between Subset Size, Step Size, and Strain Window (Filter Size) for many DIC Algorithms

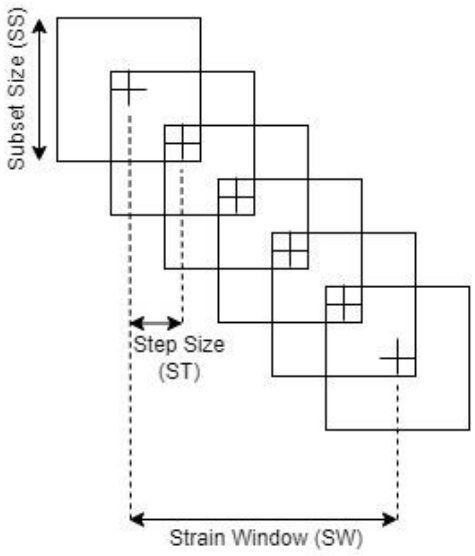

The decision on the subset size, step size, and strain window impacts the spatial strain gradient (bias errors due to smoothing) and the strain resolution (variance errors) of the strain measurement [18]. To balance the bias errors and variance errors, it is often recommended that a virtual strain gage (VSG) study be performed. The VSG represents the total number of pixels in a local region used for a strain calculation. The width of the VSG can be determined using Equation 1.2 [18].

$$VSG = \underbrace{(SW - 1)}_{\#\ of\ intervals} * \underbrace{ST}_{width\ of\ intervals} + \underbrace{SS}_{half\ a\ subset\ on\ either\ side} \quad (1.\ 2)$$

Where SS, ST, and VSG all have units of pixels, and SW has units of subsets.

Smaller VSG sizes tend to be more sensitive to noise, which can result in artificially increasing the maximum strain amplitude. Larger VSG sizes tend to reduce noise by smearing the measurement over a larger area; however, for non-uniform strains, large VSG

sizes can also increase bias errors by averaging in data from further away from the peak [11]. The VSG parameters are considered balanced when the maximum strain amplitude converges as the VSG is decreased [18]. As applied to out-of-plane bending conditions in which the specimen bends towards a pair of stereo cameras, one of the major findings of Craig et. al is that rather than relying on the strains computed by DIC, which are sensitive to all 3 parameters (SS, ST, and SW), one can get much cleaner results by fitting an analytical solution to the out-of-plane displacement (W) data and then computing strains using beam theory. The W-data is sensitive to the subset size but relatively independent of the step size and strain window [22]. Hill's method for obtaining strains in vibration-based testing adopted a similar approach [11].

One of the major challenges of DIC is maintaining sufficient lighting on the specimen, especially as applied during a vibration-based fatigue test [23]. Large out-of-plane motion necessitates the use of lenses with small aperture while high frequency vibrations require that cameras record using lower exposure times.

1.3 Lighting Methods

Over exposure of the camera sensor leads to oversaturation of the image while under exposure leads to poor contrast. To ensure sufficient contrast, the International DIC Society (iDICs) recommends at least 50 grey-scale counts between a "typical" dark feature and light feature in the speckle for an 8-bit camera [16], [18]. In 2019, Thai et al. more formally defined which values are "typical" via a normalizing metric, Δ, which describes the span of the median 90% of all greyscale values in the region of interest [24]. Figure 5 depicts a representative histogram of a region of interest for determining the Δ metric,

where z_1 and z_2 denote the 5th and 95th percentile, respectively. Jarrett et al. later extended this recommendation to other bit depths by recommending that the value of Δ should be at least 20% of the dynamic range of the camera [25].

Figure 5

Example of Evaluating the Contrast on a Test Specimen Using the Δ Metric

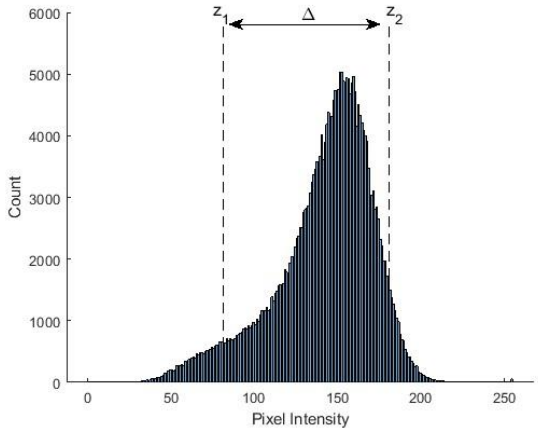

In practice, there are six main ways to control image brightness during a DIC test [26] as summarized in Table 1 [27-29], but each has important trade-offs to consider when planning a DIC measurement.

Table 1

Trade-offs in image lighting control techniques for DIC based measurements

Lighting Technique	Trade-off
(1) Increase external lighting	Increase equipment cost and can present safety concerns
(2) Increase aperture	Decrease in depth of field
(3) Increase exposure time	More susceptible to motion blur
(4) Gain	Amplified noise in images
(5) Post-Processing	Susceptible to corrupting the data
(6) Optical Filtering	Only reduces image brightness, cannot increase

External light sources (method 1 in the table) should provide flat and uniform light that is constant across the field of view and in time [18]. LED lights are an ideal source of external light due to the high intensity with minimal heat rejection [23]. LED lights with external control can be synchronized with the camera trigger to provide an intense pulse during image acquisition to further increase the brightness of the image [30]. The trade-off of high intensity lighting is the cost and safety hazards that can be introduced, such as in the case of lasers [31] and/or UV lights [28].

The aperture of the lens (method 2 in the table) governs the depth of field and how much light enters the camera [18] by imposing a physical barrier to limit the amount of light that can reach the camera sensor, as illustrated in Figure 6. The aperture blocks the outermost rays which are furthest from the optical axis, and which also contribute most to the size of the defocused zone, thereby bringing the resulting image into sharper focus. However, in blocking these rays, less total light reaches the camera sensor, resulting in

darker images. The range of distances at which the object can be placed from the camera/lens assembly and the defocused zone remains negligibly small is known as the depth of field.

Figure 6

Ray Diagram of Aperture Limiting Light Reaching Camera Sensor

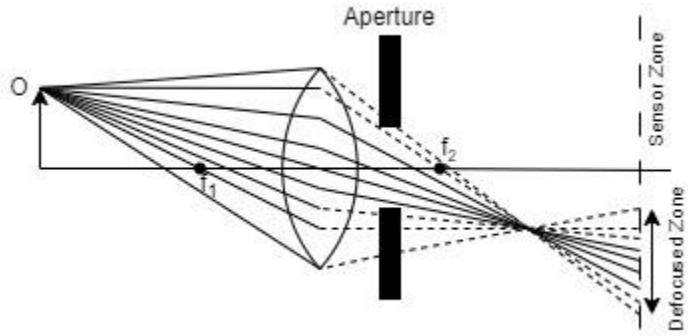

Aperture size is commonly reported in terms of an f-stop, also known as f-number. The f-stop is typically reported as a fraction such as f/11 describes the ratio the lens focal length to the diameter of the entrance pupil. For every standard increase in an f-stop, the area of the aperture is reduced in half, which allows twice as much light to be gathered on the sensor under uniform light intensity. However, at high magnifications and long working distances, small aperture sizes worsen the diffraction of light [32]. In DIC for out-of-plane bending, it is often recommended to use as small of an aperture as possible in order to increase the depth of field, resulting in less light reaching the camera sensor [33].

Exposure time (method 3 in the table) governs how long the camera sensor collects light. Longer exposure times allow more light to gather on the camera sensor, but if the object moves significantly during this time, this will result in motion blur [34], [35]. For a

periodic motion, the exposure time should be centered on the peak of oscillation to minimize the movement during image acquisition as illustrated in Figure 7.

Figure 7

Motion Blur due to Exposure Time during Image Acquisition on Periodic Motion where Δt_1 and Δt_2 are the Same Exposure Time Triggered at Different Points of the Periodic Motion

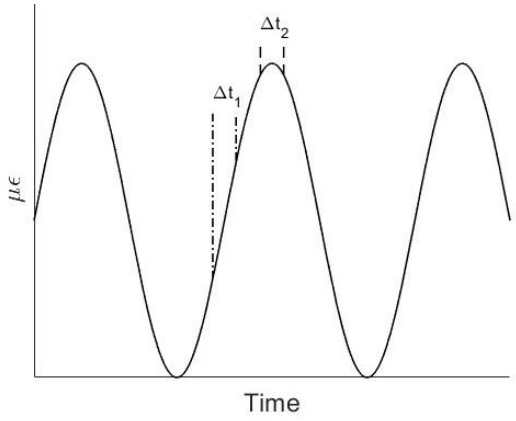

The International DIC Society (iDICs) recommends choosing an exposure time that limits the motion of the specimen during the image acquisition to the noise floor of the DIC setup (typically around 0.01 pixels of displacement). In dynamic modal tests, up to 3 pixels of motion can be acceptable [18]. For vibration-based tests, it is desired to use short exposure times to minimize the error introduced by motion blur, which results in less light reaching the camera sensor.

Camera gain (method four in the table) amplifies the entire signal, including background noise, from the camera sensor, as illustrated in Figure 8.

Figure 8

Simulation of Noise Amplification due to Introduction of Gain in Image Acquisition

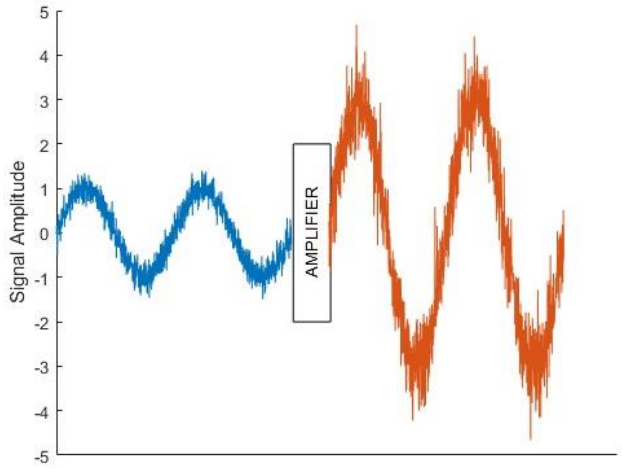

The amplification of the signal can occur either before the analog-to-digital converter (true gain) or after the analog-to-digital converter (digital gain). Digital gain uses a conversion table to map the digital values to new values [36]. The use of camera gain is generally discouraged for DIC [18] due to the increase of noise in the images, which can negatively affect the calibration and DIC matching algorithm [16]. For example, Figure 9 shows the mean and standard deviation of noise, which is computed by taking two successive images under varying levels of gain, subtracting the two images, and computing the spatial mean or standard deviation of that difference across the population of all pixels in the images.

Figure 9

(a) Mean and (b) Standard Deviation of Noise in Digital Image Captures at 30µs Exposure Time

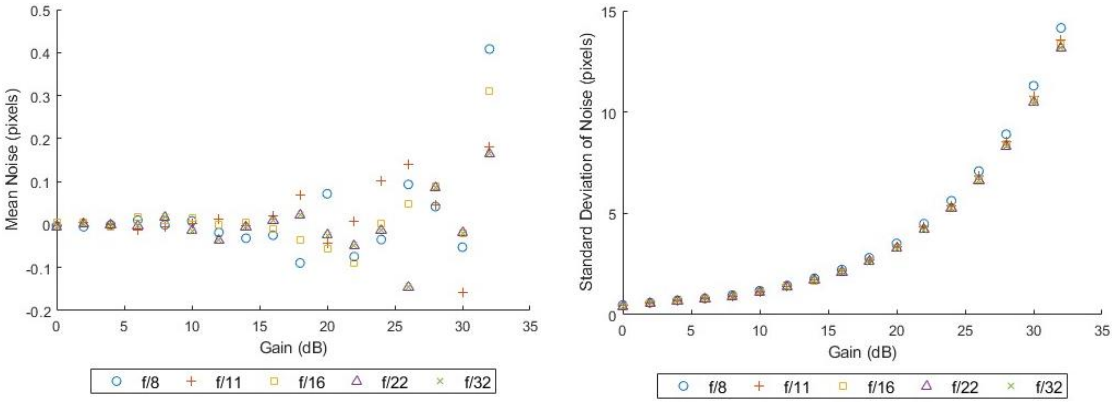

(a) (b)

Post-processing (method five in the table) can be used in very limited circumstances to artificially brighten the images or to improve contrast. For example, Archer et al. used detailed temperature and emissivity measurements to subtract unwanted light which was emitted as blackbody radiation at high temperature [29]. In quasi-static measurements at high temperature, one can average together multiple images with nominally no difference between them to reduce the effect of heat haze [37]. However, such techniques should be used very carefully, as they risk directly corrupting the measurement [26].

Filtering (method six in the table) is a technique to reduce the amount of light acquired during image acquisition. For example, in the case of high temperature DIC, a blue band-pass filter [38], [39], [40] or UV band-pass filter [28] can be used to remove the longer wavelengths emitted by a test specimen due to black body radiation, which allows for a higher temperature limit before saturating the image [41]. It should be noted that filtering will only reduce the light reaching the camera sensor. To compensate for the

reduced light, the other methods presented in the table should be adjusted to maintain the appropriate Δ level.

It is generally recommended in DIC that one should use the brightest lights safely available (method 1 in the table) and to choose aperture and exposure time (methods 2 and 3) based on experimental needs. The remaining methods should generally be avoided. However, in the case of vibration-based fatigue tests, the plate oscillates very quickly out of plane, which necessitates both small apertures (to improve depth of field) and short exposure times (to reduce motion blur) [11]. This raises the question: once the user adopts the brightest lights that they have safely available, could gain be a viable option to add more lighting to the specimen without adversely impacting the strain measurements?

1.4 Overview

In this work, the interaction of external lighting, camera aperture, camera exposure time, and camera gain is analyzed. A Design of Experiments (DOE) is conducted to determine the significant interactions between the lighting techniques and uncertainty in the DIC strain calculations. A single insert plate is driven near its “two-stripe” resonant frequency at the different camera parameters and strain levels according to the DOE test matrix. The outcome of this work quantifies the uncertainty associated with changing the aperture, exposure time, gain, or external lighting source and provide a recommendation on how to control lighting during vibration-based fatigue tests.

CHAPTER 2

OBJECTIVES

1. Determine the combination of lighting that reduces uncertainty in DIC strain measurements as applied to vibration-based fatigue testing.
2. Evaluate the difference between two external (strobe light and ring light) lighting sources.
3. Address the question, is gain ever the least worst option?

CHAPTER 3

METHODS

3.1 Sample Preparation and Equipment Setup

This work used an equipment setup similar to the work performed by Hill et al [11], except that instead of studying solid rectangular plates, this work used the Bruns, Zearley et al [8] carrier-insert assembly design, as shown in Figure 10. The carrier plates and the insert specimens were machined from 6061-T6 aluminum while the reinforcing tabs were machined from 304 stainless steel. To enable DIC, a high-contrast speckle pattern was applied to the top surface of the insert specimens using a white background with black speckles. In the fatigue zone on the bottom surface of the insert specimens, a Micro-Measurements Precision Sensors strain gage (CE-13-062UW-350) was applied in a quarter-bridge configuration. Copper wires were routed along the nodal lines to a bondable solder terminal and connected to a Vishay 2310B Signal Conditioner.

Figure 10

Bruns-Zearley Carrier-Insert Assembly Design with Applied Strain Gage and Wiring

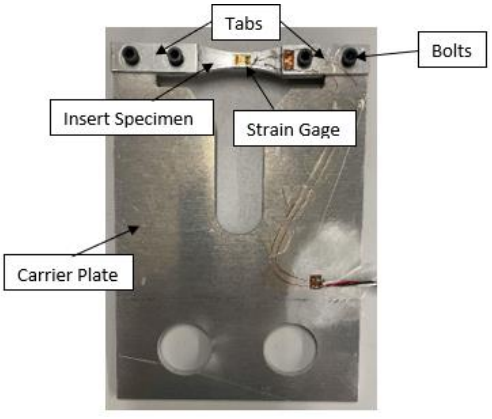

A diagram of the experimental setup is shown in Figure 11.

Figure 11

(a) Diagram of Experimental Setup and (b) Photo of Test Setup

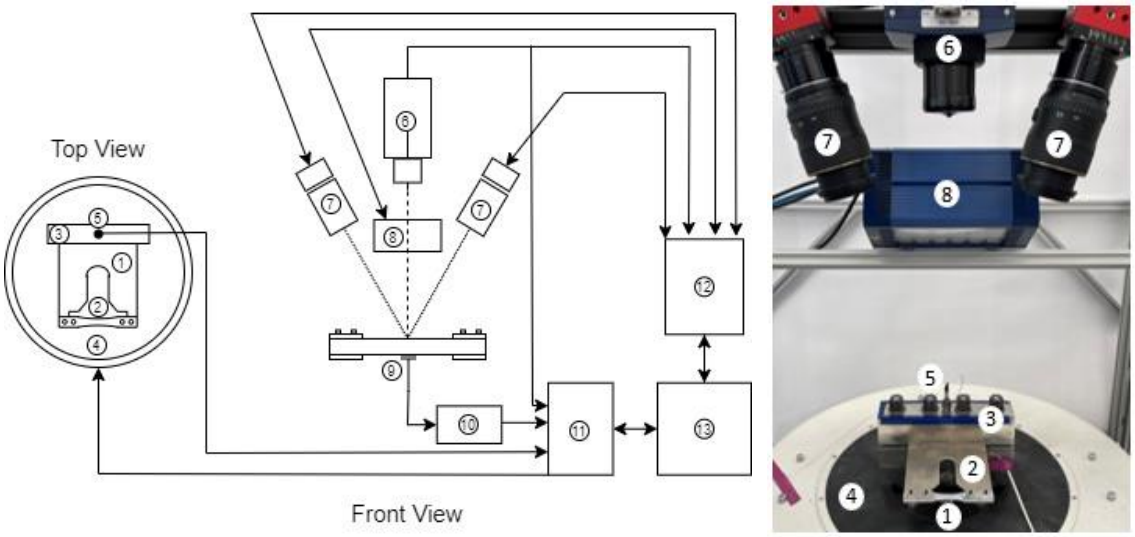

(a) (b)

Components

1 – Carrier Plate	5 – Accelerometer	8 – Strobe Light/Ring Light	11 – Shaker Controller
2 – Insert Specimen	6 – Laser Vibrometer	9 – Strain Gage	12 – DAQ
3 – Clamping Block	7 – Cameras & lenses	10 – Signal Conditioner	13 - Computer
4 - Shaker			

The carrier-insert test articles (1 and 2 in Figure 11) were cantilevered using a rigid clamping block (3) mounted above a Data Physics V-617 electrodynamic shaker (4). A Dytran 305D5T accelerometer (5) was attached to the clamping block to provide force control to the electrodynamic shaker. A Polytec OFV-505 laser vibrometer (6) was positioned near the center of the fatigue zone on the top surface of the insert specimens to create a displacement-strain calibration curve. A piece of reflective tape was applied to the top surface of the insert specimens to improve the signal to the laser vibrometer. The laser

vibrometer, accelerometer, and strain gage were connected to a Data Physics Abacus 901 controller (11).

Two Prosilica GT6600 digital cameras (7) were placed in a stereo configuration to enable 3D-DIC measurements. The cameras were mounted on a separate frame from the laser vibrometer to reduce hysteresis errors introduced by the compliance of the frame due to the manual adjusting of the aperture size during the vibration tests. The laser vibrometer and cameras were connected to a NI-DAQ USB 6251 (12) to provide phase locking capabilities similar to the procedure developed by Furman et al. [30].

Two different types of external light sources were used in this work: a pair of LED ring lights (not shown in Figure 11) from CCS Inc. and an illumiNova® strobe light (8) from Monarch Instruments. To ensure that the carrier-insert assembly remained minimally fatigued across all tests, two nominally-identical carrier-insert assemblies were created, with each dedicated to a specific light source. In one test configuration, the two CCS ring lights provided constant illumination on a test specimen. The other test configuration used a strobe light connected to the NI-DAQ to pulse simultaneously with the camera triggers. For both external light source types, the peak of oscillation was targeted for image acquisition.

VIC-3D DIC software was used to process the images captured during the vibration test. Calibration images for each aperture size tested were taken using a Correlated Solutions 14x10 reference plate with 4mm spacing prior to performing the vibration test. Images of the undeformed stationary specimen were taken at the camera parameters specified by the DOE test matrix to provide a reference image for the VIC-3D algorithm.

3.2 Test Matrix Generation

A central composite response surface DOE design with axial points [42] (shown in Figure 12) was used in Minitab to determine the effect of different exposure times and gain levels on a DIC measurement for a specified aperture size and external light source.

Figure 12

Cube Point and Axial Point Central Composite Response Surface Design Space

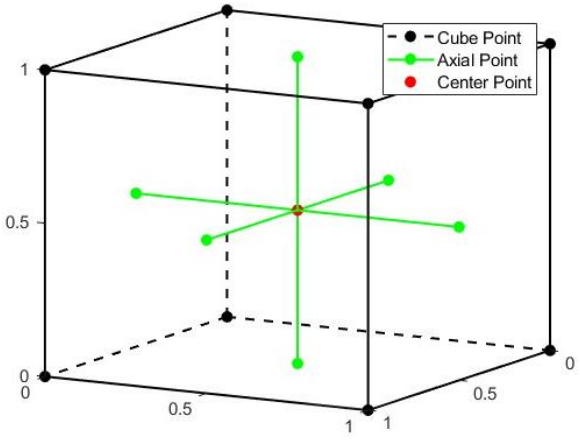

To determine the maximum and minimum aperture, exposure time, and gain settings for each external lighting source, static images were analyzed at a set aperture level by varying the exposure time and gain to determine the saturation points. For this work, three aperture sizes were considered for each external lighting method to represent a shallow, moderate, and large depth of field. Consideration was taken to allow sufficient range for varying the exposure time and gain levels without saturating the image for a given aperture size. Table 2 summarizes the high and low lighting parameters used in Minitab for generating the response surface DOE testing matrix.

Table 2

High and Low Settings used for the Central Composite Response Surface

External Lighting	Aperture	Setting	Exposure Time (μs)	Gain (dB)
Ring Light	f/5.6 (wide)	Low	80	0
		High	400	20
	f/11 (moderate)	Low	80	0
		High	400	28
	f/22 (moderate/narrow)	Low	80	0
		High	400	32
Strobe Light	f/16 (moderate)	Low	30	0
		High	150	6
	f/22 (moderate/narrow)	Low	30	0
		High	150	12
	f/32 (narrow)	Low	30	0
		High	150	15

The test matrix produced a total of 6 response surfaces: [2 light sources] x [3 apertures]. Each response surface required 13 runs of a DIC measurement, such that the full text matrix, shown in Table 3 for ring lights and Table 4 for strobe lights, involves 78 measurements of strain.

Table 3

Response Surface DOE Test Matrix for Ring Light External Lighting Condition

	Aperture 5.6		Aperture 11		Aperture 22	
Run Order	Exposure Time	Gain	Exposure Time	Gain	Exposure Time	Gain
1	240	10	240	14	353	27
2	240	20	240	14	400	16
3	240	10	80	14	80	16
4	127	3	240	14	240	16
5	400	10	400	14	240	16
6	353	3	240	0	240	16
7	80	10	127	24	240	16
8	240	10	127	4	353	5
9	127	17	240	28	240	32
10	120	0	353	4	127	27
11	240	10	353	24	127	5
12	353	17	240	14	240	0
13	240	10	240	14	240	16

Table 4

Response Surface DOE Test Matrix for Strobe Light External Lighting Condition

	Aperture 16		Aperture 22		Aperture 32	
Run Order	Exposure Time	Gain	Exposure Time	Gain	Exposure Time	Gain
1	90	3	90	6	48	13
2	90	0	90	6	90	8
3	90	3	132	2	30	8
4	48	5	132	10	90	0
5	90	3	90	6	90	8
6	90	6	90	0	150	8
7	90	3	90	12	132	2
8	150	3	90	6	90	8
9	90	3	90	6	90	15
10	132	5	48	2	132	13
11	48	1	30	6	90	8
12	30	3	150	6	48	2
13	132	1	48	10	90	8

3.3 Experimental Procedure

Due to the different external lighting conditions, the testing was split into two groups: ring light and strobe light. The two test groups used different carrier-insert assemblies to avoid premature failure during testing. Both test groups were performed in three stages: (1) a frequency sweep to identify the resonant frequency of the two-stripe mode, (2) the generation of a strain-displacement calibration curve, and (3) a series of 78 dwell tests at $2250\mu\epsilon$ using the surface response test matrix in Table 3 and Table 4.

First, the frequency of the two-stripe resonant mode was found by performing a broad frequency sweep followed by a narrower, more precise frequency sweep, as shown in Figure 13. The two-stripe resonant frequency for ring light and strobe light test specimen were 909.5 Hz and 908 Hz, respectively.

Figure 13

(a) Broad and (b) Narrow Two-Stripe Frequency Search for the Ring Light Carrier-Insert Plate and (c) Broad and (d) Narrow Frequency Search for the Strobe Light Carrier-Insert Plate

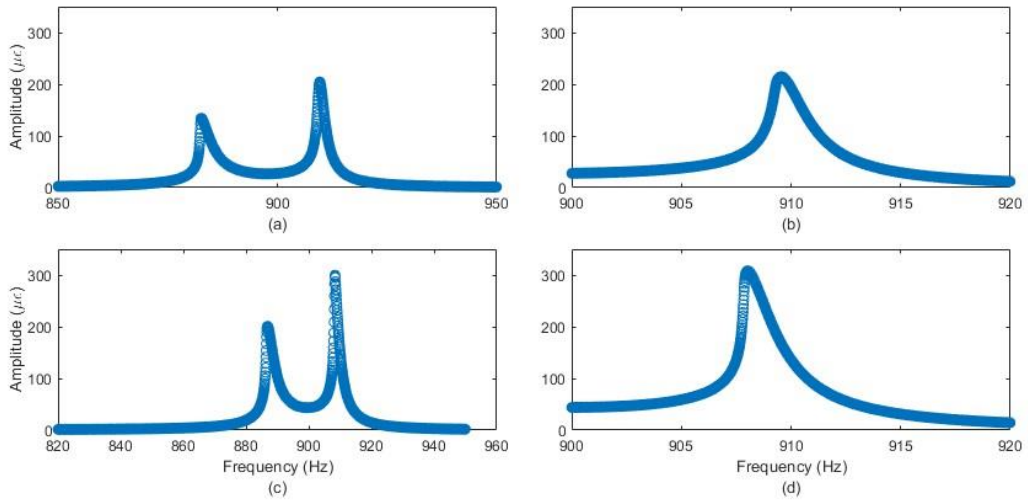

Second, a strain-displacement calibration curve (Figure 14) was generated for both test specimens by specifying the shaker excitation level and recording the strain from the strain gage and the displacement measured by the laser vibrometer. The procedure is comparable to the one used by Hill et al [11], except the displacement as measured by the laser vibrometer was calibrated against the strain gage instead of the velocity. The displacement measurement was used to eliminate the dependency of the strain measurement on the frequency of the fatigue test. Near the end of a fatigue test, fatigue damage leads to a slow decrease in natural frequency. If tests are controlled using velocity measurements, the decrease in frequency can lead to an increase in strain amplitude. The coefficients of the linear fit were determined by using the matrix solution presented by Bevington and Robinson [43].

Figure 14

Strain-Displacement Calibration Curve for (a) Ring Light and (b) Strobe Light Carrier-Insert Plates

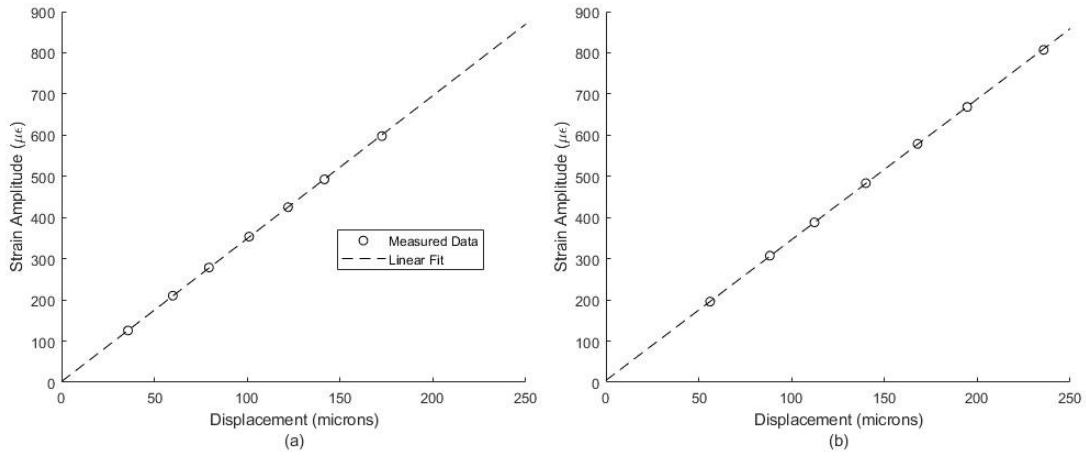

Third, images were captured using the lighting parameters specified by the response surface test matrix when the carrier-insert specimen was subjected to a 2250$\mu\epsilon$ excitation. This excitation is comparable to, yet slightly below, those used in similar vibration-based tests [8] such that the risks of motion blur due to overly long exposure times and/or poor depth of field due to overly wide apertures is comparable to the risks expected in those tests. The excitation is slightly reduced such that fatigue damage remains negligible across all 39 strain measurements for a given light source, such that all measurements are performed at nominally the same strain.

Image capturing began approximately 20 seconds after the excitation level is reached to allow the plate to reach steady-state conditions [11]. Since the gain and exposure time can be remotely controlled using the phase locking program developed by Furman et al. [30], the camera settings were adjusted without pausing the vibration test. After the image acquisition for all the tests for aperture size, the vibration test was paused to change the aperture setting on the cameras. The excitation was resumed, and the next set of images was captured.

Following the experiments, the images were processed in VIC-3D to calculate full-field W-displacements. To facilitate a more direct comparison of the effect of exposure time and gain on the end strain result, one subset size was used for all VIC analysis. The subset size was determined by using a bracketing approach to a VSG study while following the general procedure recommended by iDICS [18]. This bracketing approach varied the subset size for the lowest and highest delta values from the extreme aperture cases for both lighting methods. For this work, the strain window and step size were not varied because subsequent strain calculations were based on the raw W-displacement, not the strains as

computed by VIC-3D. Figure 15 shows that the majority of the data points first stabilize at a subset size of 39, as such, this subset size was adopted for this work.

Figure 15

Bracketing VSG Study to Determine Subset Size for VIC Analysis on all DOE Tests

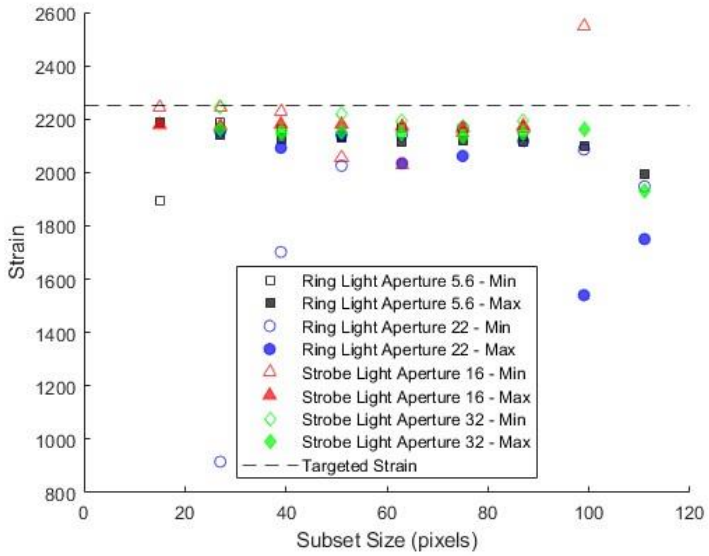

CHAPTER 4

RESULTS

Representative images of the range of lighting (minimum and maximum delta) on the test specimen for each of the aperture sizes (see Table 3) used in the ring light and strobe light testing configuration are shown in Figure 16 and Figure 17, respectively.

Figure 16

Difference in Lighting on the Ring Light Test Configuration for the Different Aperture Sizes: Wide (a) Min Δ (b) Max Δ,Mmoderate (c)Min Δ (d) Max Δ, and Narrow (e) Min Δ (f) Max Δ

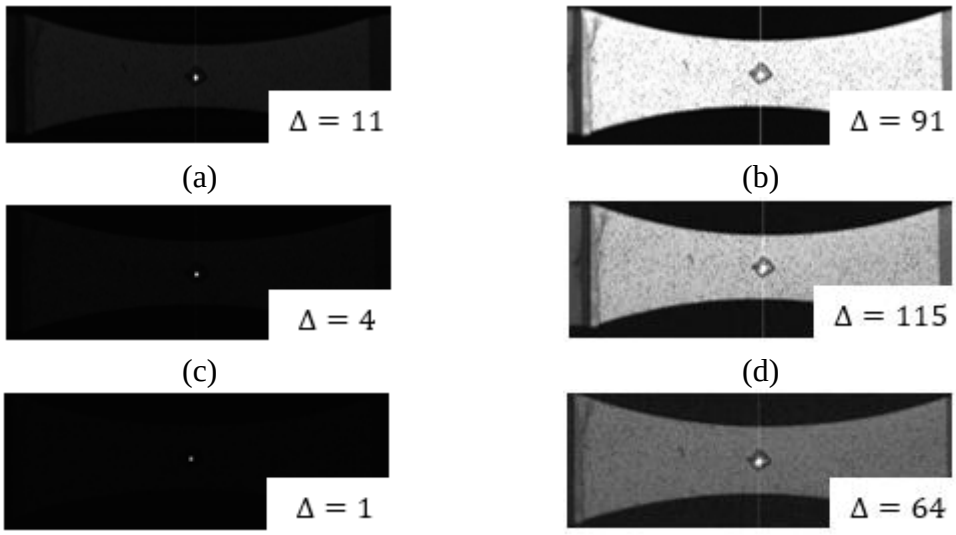

Figure 17

Difference in Lighting on the Strobe Light Test Configuration for the Different Aperture Sizes: Wide (a) Min Δ (b) Max Δ, Moderate (c) Min Δ (d) Max Δ, and Narrow (e) Min Δ (f) Max Δ

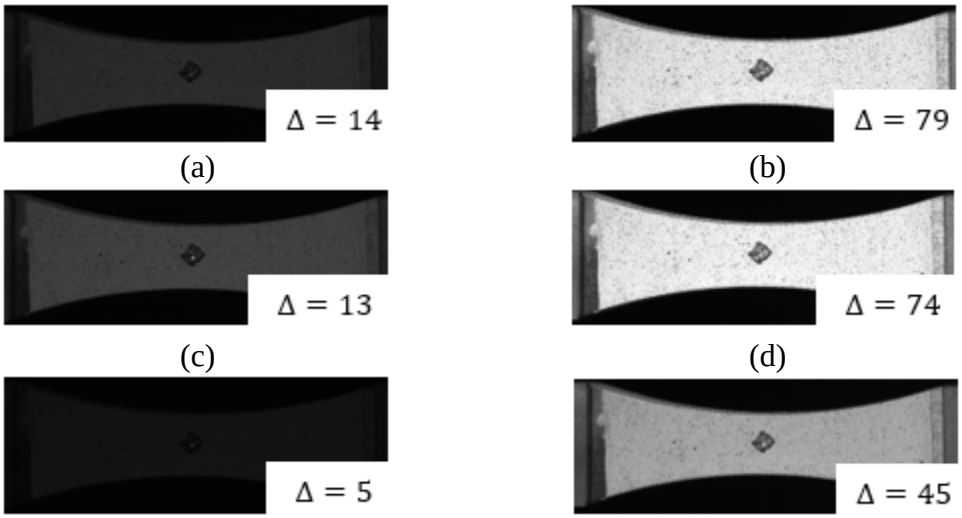

The W-displacements from VIC-3D were fit to a surface using a variation of the Euler-Bernoulli beam curve solution for an hourglass shaped specimen developed by Furman et al. [44]. The method used in this work uses a regression of the W-displacement data to solve the beam equation instead of using the material and geometric constants in conjunction with the W-displacement data. Figure 18a shows a representative example of the W-data from the VIC-3D measurement compared to the fit of the W-displacement using the Euler-Bernoulli solution method. For a more direct comparison for the strain from the Euler-Bernoulli solution to the strain from the displacement-strain calibration curve, the Euler-Bernoulli strain was averaged across the physical strain gage region. A representative example of the strain surface generated by the Euler-Bernoulli solution with the region averaged to represent the strain gage is shown in Figure 18b.

Figure 18

Representative Examples of (a) Euler-Bernoulli Fit to the Raw DIC W-data and (b) Resulting Euler-Bernoulli Strain Surface with Physical Strain Gage Region Superimposed

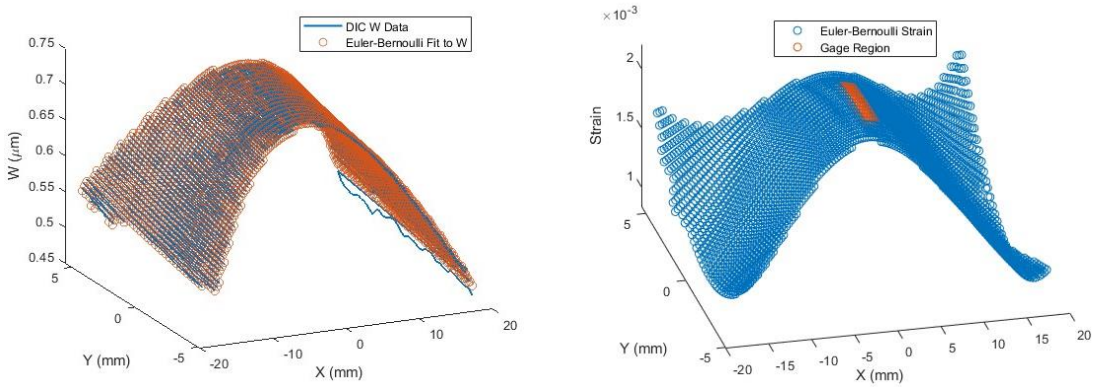

The images (30 stereo image pairs for each strain measurement to match the procedure by Hill et al. [11]) captured during one of the tests were averaged at each point across the images to reduce the impact of noise on the VIC-3D measurement. In Hill's work, it was determined that there was no significant difference in the resulting strain measurements if the W-displacement data from VIC-3D was spatially averaged before calculating the strain or if the strain was spatially averaged at the end. In this work, the W-displacement data was averaged prior to strain calculations to reduce the computational power.

To enable comparison between the strains between the different tests in Table 3 and Table 4, the Euler-Bernoulli strain was compared against the extrapolated strain from the displacement-strain calibration curve using the percent absolute relative error equation as described in Eq 4.1.

$$\%RE = \left|\frac{\bar{x}_{SG} - \bar{x}_{EB}}{\bar{x}_{SG}}\right| * 100\% \quad (4.1)$$

Where %RE is the absolute percent relative error, $\bar{x}_{SG}$ is the extrapolated strain from the strain-displacement calibration curve, and $\bar{x}_{EB}$ is the strain from the Euler-Bernoulli DIC solution. Representative examples of the displacement measured by the laser vibrometer during the vibration test are shown in Figure 19, with the gray regions representing the time for which images were not captured to allow the plate to reach steady state conditions. The spikes seen in Figure 19 are due to the momentary correction of the shaker control loop to maintain a certain phase angle. Since the spikes are due to the shaker control feedback loop, the frequency or magnitude of the spikes is not a result of different lighting conditions, but rather a reflection of shaker output during a test. In a normal fatigue test, these spikes can be problematic because they lead to premature failure of the test specimen, but they are based on the feedback control provided by the laser vibrometer and have nothing to do with the camera-based measurements. In this work, the spikes do not significantly influence the mean strain measurement because the W-displacement data is averaged over approximately 30 image pairs.

Figure 19

Displacement Reading from the Laser Vibrometer during (a) Ring Light Wide Aperture and (b) Strobe Light Moderate Aperture Dwell Tests. Shaded Regions Represent Time Allowed for Plate to Reach Steady-State Conditions where no Images were Captured

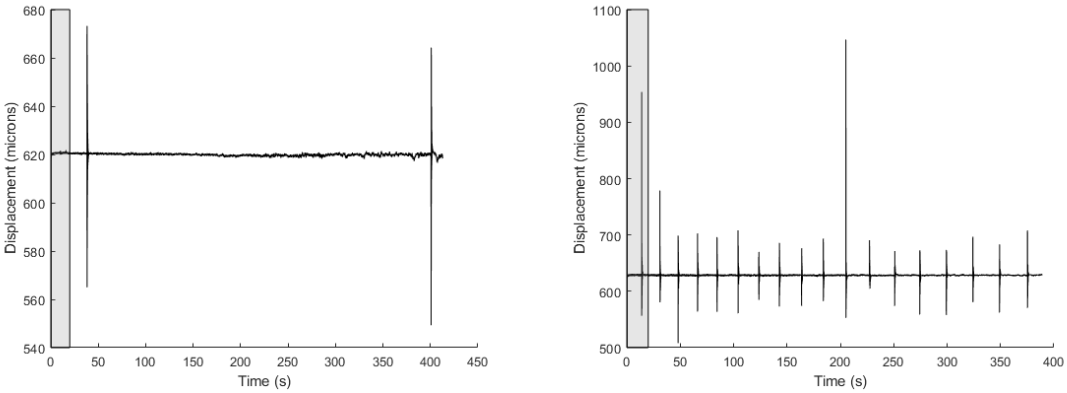

(a) (b)

The average extrapolated strain from the displacement reading by the laser vibrometer for each aperture size is summarized in Table 5. The tests for a specific aperture size were run without interruption of the shaker (gain and exposure time were altered remotely), so the strain as determined by the laser vibrometer applies to all the tests for that aperture size. However, the strains determined from the Euler-Bernoulli solution are test specific.

Table 5

Average Strain Extrapolated from the Strain-Displacement Calibration Curve

External Light Source	Aperture Size	Strain ($\mu\epsilon$)
Ring Lights	f/5.6 (wide)	2154.31
	f/11 (moderate)	2154.28
	f/22 (moderate/narrow)	2155.30
Strobe Lights	f/16 (moderate)	2151.70
	f/22 (moderate/narrow)	2150.99
	f/32 (narrow)	2151.13

Contour plots of the percent relative error between the strain as extrapolated from the laser vibrometer and the Euler-Bernoulli DIC fit are shown in Figure 20 for the ring light and strobe lights with the test points from Table 3 and Table 4 represented as points on the contour. It should be noted that the exposure time is consistent within an external light source, but the gain axis varies based on the saturation limit of the aperture size. The bottom left corner of each plot represents the lowest lighting condition, while the upper right corner of the contour plot represents the brightest lighting condition. For both external light sources, the contour plots suggest the absolute percent relative error is relatively insensitive to the gain level, as evident by the vertical nature of the contour lines, and most sensitive to the exposure time for the min and mid aperture sizes. The darkest aperture settings for both external light sources exhibit primary sensitivity to the exposure time with a smaller, secondary sensitivity to the gain level, as evident by the curvature of the contour lines.

Figure 20

Percent Relative Error between Peak Strain Measured from Strain from the Calibration Curve for the Ring Lights (a) Wide, (b) Moderate, (c) Moderate/Narrow and Strobe Lights (d) Moderate, (e) Moderate/Narrow, and (f) Narrow. Test Lighting Configurations are shown as Black Points

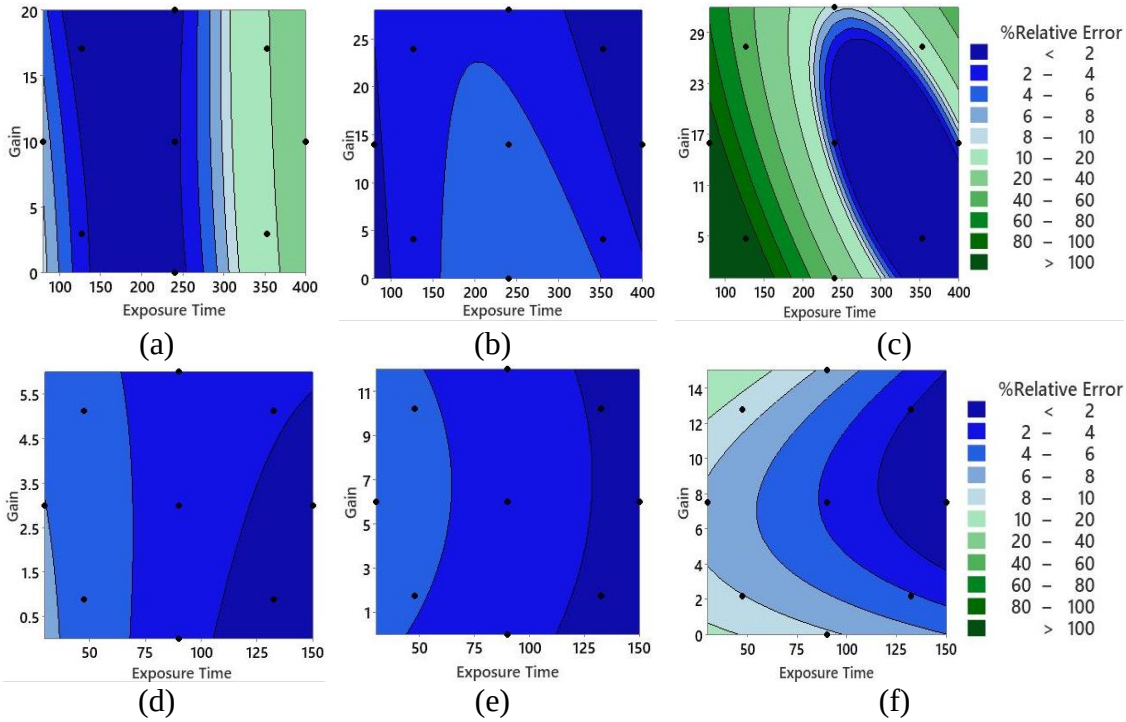

In addition to agreement with respect to the extrapolated strain from the laser vibrometer, the stability of the strain measurement can be assessed by the width between two adjacent contour lines. The ring light wide aperture shows good stability at the center of the exposure time range, as evident by the large contour region, but exhibits instability moving away from the center by narrow contour regions. The ring light moderate aperture shows good stability throughout the exposure time range while the ring light moderate/narrow aperture shows instability until high levels of exposure time are used. The strobe light moderate and moderate/narrow apertures show similar stability by having few

contours across the exposure time range while the strobe light narrow aperture exhibits lower stability comparatively.

4.1 Discussion of Results

The contour plot shown in Figure 20 shows the strobe light are generally preferable to the ring lights because the strobe lights exhibit better stability (wider contour bands) and large regions of accuracy with the extrapolated strain from the laser vibrometer. This supports the general advice to use the brightest light sources that are safely available [26]. When brighter light sources are not available, the contour plots in Figure 20 suggest dimmer light sources can still produce quality data, but the tradeoffs between aperture size, exposure time, and gain must be more carefully examined to ensure stable, quality measurements.

When the external light source is sufficiently bright, as is the case for the strobe light contour plots in Figure 20d-f support the recommendation to reduce the aperture size to improve the depth of field [18] up to a point. After passing the moderate depth of field apertures, narrowing the aperture further tends to destabilize the measurement without providing improved accuracy. When the external light source is relatively dark, as is the case for the ring light contour plots in Figure 20a-c, choosing the appropriate depth of field becomes more critical. An aperture size that is too wide or too narrow, as seen in Figure 205a and Figure 20c, leads to instability in the measurement and can produce large errors in the measurement.

In general, the contour plots in Figure 20 illustrate the percent relative error between the Euler-Bernoulli strain solution and the extrapolated strain data from the laser

vibrometer is most sensitive to the exposure time and relatively insensitive to the gain level. This is evident by the vertical nature of the contour lines with only a slight curvature in the horizontal direction. When a wide aperture is used, as seen in Figure 20a, short and long exposure times lead to instability and large errors in the measurement. For this case, mid-range exposure times should be used for the best agreement with the extrapolated strain. The moderate and narrow aperture sizes, shown in Figure 20b-f, benefit from longer exposure times.

The wide and moderate aperture sizes show little sensitivity to the gain level, as seen in Figure 20a-b and Figure 20d-e. Gain becomes a useful tool only when narrow apertures are required for a test, as seen in Figure 20c and Figure 20f. However, as previously discussed, narrowing the aperture to increase the depth of field is not beneficial after the moderate aperture sizes. As such, it is generally unnecessary to use gain. Instead, the external light source, aperture size, or exposure time should be modified to improve the strain measurement.

CHAPTER 5

UNCERTAINTY

The uncertainty associated with the extrapolated strain from the calibration between the strain gauge and laser vibrometer is not included in this analysis because the object of this work is to compare the effect of lighting conditions on the resultant strain measurement. The purpose of the strain gage was to provide a baseline reference for comparing the average strains between the different lighting sources. A detailed uncertainty analysis with considerations to the extrapolated strain is presented in Appendix A as a supplementary analysis.

In this work, the uncertainty associated with a lighting condition was quantified by performing a Monte-Carlo Method (MCM) uncertainty propagation [43] on the Euler-Bernoulli derived strain. The MCM simulates thousands of potential results based on the individual uncertainties of the input arguments of a data reduction equation. The quantity of interest for this work is the tolerance range (difference between 95th percentile and 5th percentile) of the absolute percent fluctuation around the mean strain, as calculated by Equation 5.1.

$$u_{x_i} = \left|\frac{\bar{x} - x_i}{\bar{x}}\right| * 100\% \tag{5.1}$$

where u_{x_i} is the uncertainty in a single Monte-Carlo simulation, $\bar{x}$ is the mean strain of all simulations, and x_i is the strain from a single Monte-Carlo simulation.

Four sources of uncertainty in the Euler-Bernoulli solution are recognized in this work: the radius of curvature of the test specimen (r), thickness of the test specimen (h_0),

minimum width of the test specimen (b_0), and the subset size determined from the VSG study. The tolerance on the insert specimen drawing was assumed to be the uncertainty range for r. The uncertainty of h_0 was determined by calculating the standard deviation of the thickness after 20 measurements a digital micrometer and combining that uncertainty with the resolution uncertainty of the micrometer by using Eq 5.2. The uncertainty of b_0 was determined in a similar fashion but using calipers instead of a micrometer.

$$u_i = \sqrt{u_{xource1}^2 + u_{source2}^2 + u_{source3}^2 + \cdots} \qquad (5.2)$$

From the VSG study (Figure 15), it is observed that there is a small change in strain if the subset size is varied around the chosen subset size of 39. For completeness, it is desired to include an uncertainty surrounding choosing a different subset size. Since the subset size constitutes a different DIC dataset, to perform the MCM the dataset of the subset size of interest was loaded and then the geometric parameters were varied according to their uncertainties. The nominal values and associated uncertainties for the parameters used in the Euler-Bernoulli strain analysis are described in Table 6.

Table 6

Nominal and Uncertainty Range for the Insert Specimen Geometric Properties

Light Source	r (in.)	h_0 (in.)	b_0 (in.)	SS (pixels)
Ring Lights	2.313 ± 0.003	0.122 ± 0.0004	0.2570 ± 0.0027	35, 39, 43
Strobe Lights	2.313 ± 0.003	0.121 ± 0.0006	0.2570 ± 0.0025	35, 39, 43

The Monte-Carlo analysis was performed using 10,000 different simulations. Examples of the resulting strain distributions are shown in Figure 21. Because the

uncertainty is being measured as an absolute percent difference, there is a bound at zero. The different distributions are a direct cause from the subset size selection. In Figure 21a, the subset size selection does not have a significant impact on the distribution but does widen the distribution. This is the most desirable case because of the single distribution that is biased towards zero. In Figure 21b, the distribution is bi-modal due to the slight difference in the strains between different subset sizes. This difference tends to have a more significant effect of widening the tolerance range than seen in Figure 21a. In Figure 21c, the selection of the subset sizes drastically influences the final strain results and leads to a large tolerance window.

Figure 21

Representative Samples of MCM Simulations for Uncertainty Analysis taken from (a) Strobe Light with Moderate Aperture Size, Mid-Length Exposure Time, and High Gain (b) Strobe Light with Moderate Aperture, Long Exposure Time, and Low Gain, and (c) Ring Light with Narrow Aperture, Mid-Length Exposure Time, and High Gain

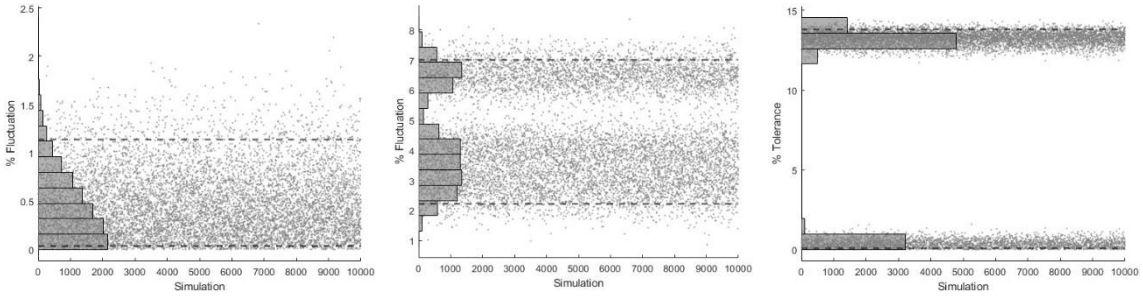

(a) (b) (c)

The tolerance range was input in Minitab as a response to the DOE test matrix to analyze the effect of gain and exposure time for each aperture size on the uncertainty. As defined this way, a smaller tolerance range is desirable because it indicates less sensitivity in the measurement with respect to the test specimen geometry and subset size selection.

The contour plots of the DOE analysis on the tolerance range with respect to exposure time and gain is shown in Figure 22 for the ring lights (plots a-c) and strobe lights (plots d-f). The contour color scale for all contour plots to facilitate comparison. The same considerations taken for interpreting the contour plots in Figure 22 should be used here.

Figure 22

Tolerance Ranges from MCM Uncertainty Analysis for Ring Lights (a) Wide, (b) Moderate, (c) Moderate/Narrow, and Strobe Lights (d) Moderate, (e) Moderate/Narrow, and (f) Narrow. Test Lighting Conditions from Table 3 and Table 4 are shown as Black Points

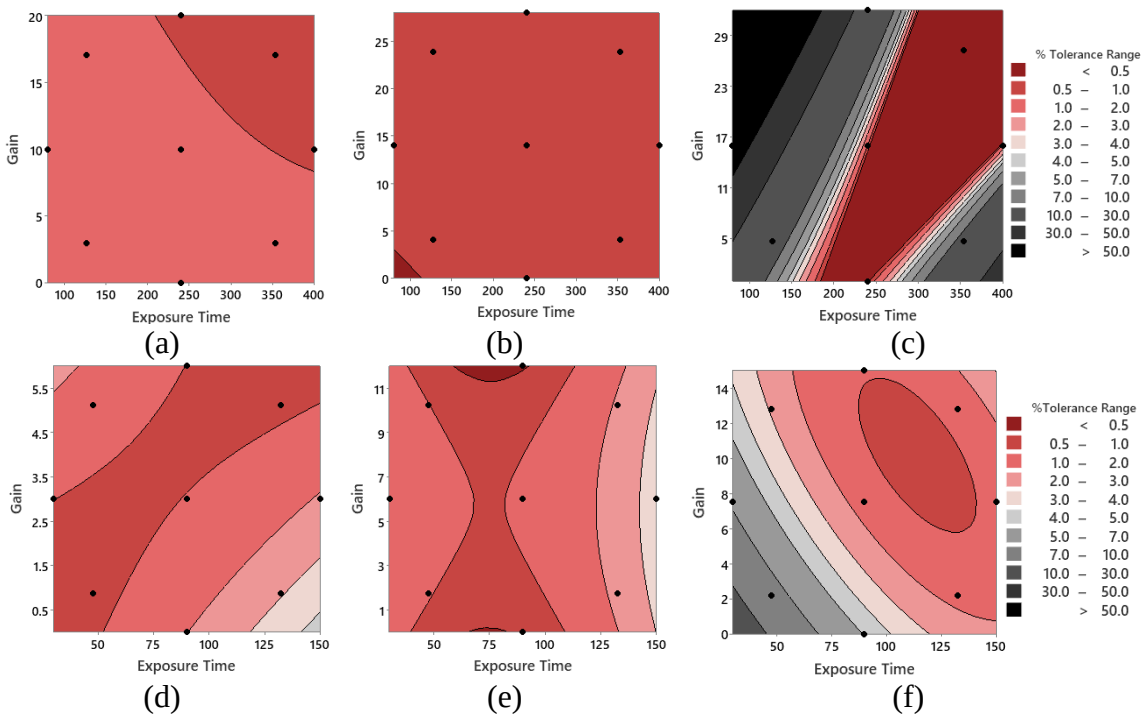

The contour plots ring lights for the wide and moderate aperture sizes are largely insensitive to the gain level and exposure time, as evidenced by the few contour lines, and have a small tolerance range. The moderate/narrow aperture size exhibits some sensitivity to the gain level, especially at higher exposure times, but is predominantly influenced by

the exposure time. The width of the contour bands for the ring lights suggest that the tolerance range is stable for the wide and moderate apertures. The moderate/narrow tolerance range shows stability at increased exposure time and gain levels but becomes unstable as exposure time decreases.

The strobe light contour plots (plots d-f) suggest that the moderate and narrow aperture sizes have a higher sensitivity to the gain level, as evident by the diagonal nature of the contour lines, while the moderate/narrow aperture size is comparatively less sensitive to the gain level. The apertures moderate and moderate/narrow show similar levels of stability, while the narrow aperture shows a slightly increased level of instability in the middle of the exposure time range.

5.1 Discussion of Uncertainty

The contour plots in Figure 22 show that the ring lights are preferable to the strobe lights for the wide and moderate aperture sizes because of the better stability and the large regions of where the tolerance range is small. The exception to this generalization is for the narrow aperture size where the strobe light demonstrates better stability than the ring lights. This is opposite of the result discussed in Chapter 4 where the strobe lights were preferable due to the better stability and accuracy with respect to the extrapolated strain.

For both external light sources, Figure 22a-b and Figure 22d-e support the recommendation to reduce the aperture to improve the depth of field up to a point. The benefit of increasing the depth of field for the strobe lights is relatively minimal because the two aperture sizes are both in the moderate and moderate/narrow category. However,

after passing the moderate depth of field apertures, narrowing the aperture further tends to destabilize and expand the tolerance range, which is undesirable.

In general, the tolerance contour plots show the tolerance range is primarily sensitive to the exposure time with a secondary sensitivity to the gain level. For a narrow aperture size, as shown in Figure 22a, modifying the gain level in conjunction with longer exposure times is required to achieve the smallest tolerance range. For the moderate aperture sizes, short to mid-length exposure times lead to the smallest tolerance range while long exposure times tend to increase the tolerance size when the strobe light is used as the external light source. The narrowest aperture for each external light condition require long exposure times and increased gain levels to reduce the tolerance range.

The gain plays a secondary role in influencing the tolerance range. For the narrow aperture size shown in Figure 22a, the only way to reduce the tolerance range is to increase the gain level. Figure 22c demonstrates the worst-case lighting condition is to start with a dim light source, limit the amount of light by using a narrow aperture size and exposure time, and then utilizing gain to try and compensate for the lack of light.

CHAPTER 6

DISCUSSION

The combined results from Figure 20 and Figure 22 show that there is a tradeoff between the ring lights and strobe lights as external light sources. The strobe lights tend to have more stable results and larger regions of agreement between the Euler-Bernoulli strain solution and the extrapolation of the strain from the laser vibrometer. However, the ring lights tend to be superior for stability and minimization of the tolerance range. The exception to this generalization is the narrowest aperture size for the ring lights that exhibits instability in both the strain measurement and the tolerance band. As such, when choosing an external light source, the agreement and tolerance range should be considered. The best balance comes from following the recommendation to choose the brightest light source available because of the better stability and agreement with respect to the extrapolated strain while still providing small tolerance ranges.

The uncertainty analysis and strain results agree narrowing the aperture size to improve the depth of field is beneficial up to the moderate aperture size. Narrowing the aperture size further leads to instability in both the strain measurement and the tolerance range while creating the potential for large error and tolerance bands on the strain measurement. When the light source is dim, it is important to get the right moderate depth of field as too wide an aperture can also result in large errors in the strain measurement.

In general, a tradeoff also occurs between the strain measurement and the uncertainty for the exposure time range. As seen in Figure 20, the strobes lights had the best agreement with the extrapolated strain at longer exposure times. However, the

uncertainty analysis in Figure 22 shows that the longer exposure times tend to increase the tolerance range for the strain measurement. The narrow aperture size of the ring light exhibits a similar trade-off. In this case, a mid-length exposure time provides the best accuracy to the extrapolated strain, but longer exposure times provided the smallest tolerance range. The narrowest aperture size of both external light conditions both benefited from higher exposure times, but as previously discussed, the narrowed aperture to increase the depth of field is not desirable due to the large errors and instability that is possible.

As discussed in Chapter 4, the gain does not play a significant role in the strain measurement. In Chapter 5, the uncertainty analysis shows the tolerance range is primarily sensitive to the exposure time with a secondary sensitivity to gain. In general, there is little benefit to modifying the gain level and the larger benefits come from balancing the external light source, aperture size, and exposure time. The gain can have severe negative impacts on the measured strain and uncertainty when gain is used to overcome dim lights, narrow apertures, and short exposure times, as seen in Figure 20f and Figure 22f.

To further aid in comparison between the different aperture sizes for a light source, the percent relative errors were plotted against the normalizing delta metric, as shown in Figure 23. Using the delta metric as a common axis allows for the different aperture sizes to be plotted on the same figure. Figure 23 shows a limited range the absolute percent relative error to remove the extreme outliers (>40) and give more definition to most of the data points. This limited range removed three of the ring light moderate/narrow aperture data points that had low exposure time and large gain values. The strobe light plot there is an initial benefit to increasing delta but then the measurements are fairly stable and not

significantly influenced by additional increases to delta. The ring lights exhibit significant variation in the percent relative error for a similar delta value.

Figure 23

Absolute Percent Relative Error with Respect to the Delta Metric for (a) Ring Light and (b) Strobe Light

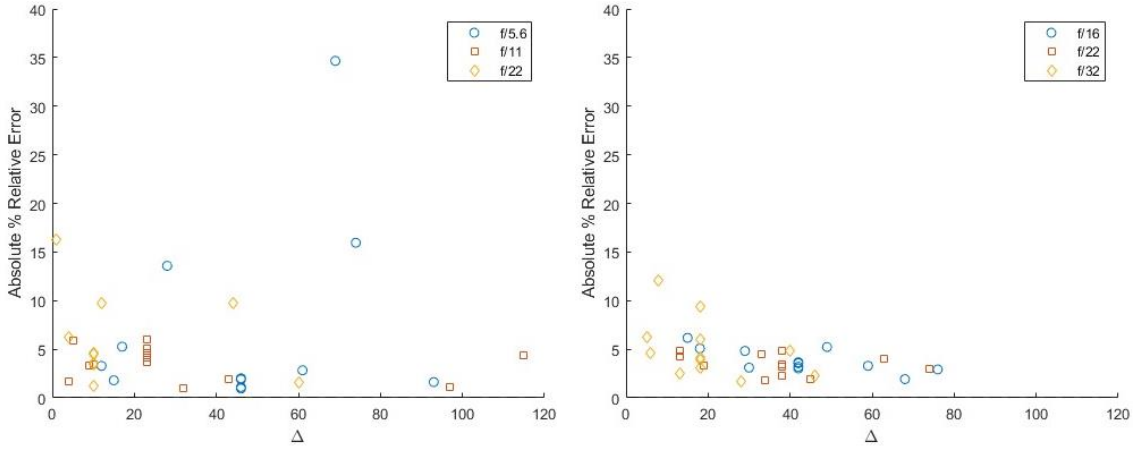

(a) (b)

Figure 24 examines the correlation between delta and the tolerance range. Both external light sources are largely insensitive to the delta metric, but there is an initial benefit to the uncertainty range by increasing the delta metric on the image. The strobe lights show a slight increase in variation in the uncertainty range at higher delta values. The ring light aperture moderate/narrow aperture size shows the most significant variation, but the variation is random with respect to the delta metric. The combined analysis of the mean strain and tolerance range results with repect to delta suggests the guidance of having a delta value greater than 50 breaks down when gain is used as a technique to improve the

delta metric. This observation suggests the source of illumination on the images should also be considered alongside the delta metric.

Figure 24

Tolerance Range for (a) Ring Lights and (b) Strobe Lights with Respect to Δ

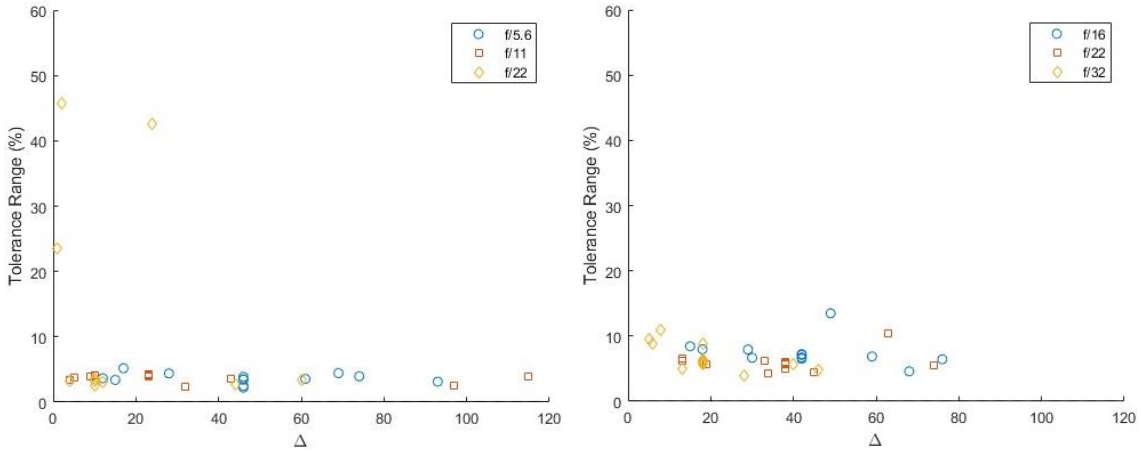

(a) (b)

CHAPTER 7

CONCLUSION

In summary, the tradeoff in lighting between aperture size, gain, exposure time, and two external lighting sources (ring lights and strobe lights) for a vibration-based fatigue test was examined using a response surface DOE design. The resulting strain from the Euler-Bernoulli strain solution using the W-displacement from DIC was compared to the extrapolated strain from a laser vibrometer to facilitate comparison between the different test lighting configurations. The comparison between the two external lighting sources shows the brighter light source (strobe lights) have better agreement with the extrapolated strain, but the dimmer light source (ring lights) have lower tolerance ranges associated with the strain measurement. The brighter light source proved most favorable at balancing the agreement with the extrapolated strain while providing acceptable tolerance ranges. Narrowing the aperture size is beneficial up to the moderate aperture range; further narrowing of the aperture size destabilizes the strain measurement and tolerance range while also creating the possibility of large errors and tolerance bands. Within an aperture size, the exposure time is the most influential factor for the measured strain and the tolerance range. However, a tradeoff exists between measured strain and tolerance range with respect to exposure time as the exposure time for the optimal measured strain tends to result in suboptimal tolerance ranges and vice versa. The measured strain was primarily insensitive to the gain level and the tolerance range was only secondarily sensitive to the gain level. In general, there is little benefit to increasing the gain level, but it is generally not detrimental. However, using gain to compensate for low light conditions from dim

external lights, narrow apertures, and short exposure times leads to significant disagreement with the extrapolated strain and large tolerance bands.

REFERENCES

[1] J. Carr, J. Baqersad, C. Niezrecki, P. Avitabile, and M. Slattery, "Dynamic stress-strain on turbine blades using digital image correlation techniques Part 2: Dynamic measurements," presented at the IMAC, pp. 221–226. doi: 10.1007/978-1-4614-2422-2_21.

[2] D. Walls, R. deLaneuville, and S. Cunningham, "Damage tolerance based life prediction in gas turbine engine blades under vibratory high cycle fatigue," *Engineering for Gas Turbines and Power*, vol. 119, no. 1, pp. 143–146, Jan. 1997, doi: 10.1115/1.2815538.

[3] W. Zhao, Y. Li, M. Xue, P. Wang, and J. Jiang, "Vibration analysis for failure detection in low pressure steam turbine blades in nuclear power plant," *Eng. Fail. Anal.*, vol. 84, pp. 11–24, Feb. 2018, doi: 10.1016/j.engfailanal.2017.10.009.

[4] M. Aykan and M. Çelik, "Vibration fatigue analysis and multi-axial effect in testing of aerospace structures," *Mech. Syst. Signal Process.*, vol. 23, no. 3, pp. 897–907, Apr. 2009, doi: 10.1016/j.ymssp.2008.08.006.

[5] R. Budynas, J. Nisbett, and K. Tangchaichit, *Shigley's Mechanical Engineering Design*, 10th ed. McGraw Hill Education, 2016.

[6] R. Berke, B. Furman, C. Holycross, and O. Scott-Emuakpor, "Damage Accumulation in a Novel High-Throughput Technique to Characterize High Cycle Fatigue," *J. Test. Eval.*, vol. 49, no. 1, Jul. 2020, doi: 10.1520/JTE20190593.

[7] T. J. George, J. Seidt, M.-H. Herman Shen, T. Nicholas, and C. J. Cross, "Development of a novel vibration-based fatigue testing methodology," *Int. J. Fatigue*, vol. 26, no. 5, pp. 477–486, May 2004, doi: 10.1016/j.ijfatigue.2003.10.012.

[8] J. Bruns, A. Zearley, T. George, O. Scott-Emuakpor, and C. Holycross, "Vibration-Based Bending Fatigue of a Hybrid Insert-Plate System," *Exp. Mech.*, vol. 55, no. 6, pp. 1067–1080, Jul. 2015, doi: 10.1007/s11340-015-0004-6.

[9] T. J. George, M.-H. H. Shen, O. Scott-Emuakpor, T. Nicholas, C. J. Cross, and J. Calcaterra, "Goodman Diagram Via Vibration-Based Fatigue Testing," *J. Eng. Mater. Technol.*, vol. 127, no. 1, pp. 58–64, Feb. 2005, doi: 10.1115/1.1836791.

[10] B. A. Furman, B. D. Hill, E. E. German, O. Scott-Emuakpor, and R. B. Berke, "Shape Optimization of Rectangular Plates for Vibration-Based Fatigue Testing," *J. Appl. Mech.*, vol. 88, no. 9, Apr. 2021, doi: 10.1115/1.4050676.

[11] B. Hill, B. Furman, E. German, J. Rigby, and R. Berke, "Non-contact strain measurement to eliminate strain gages in vibration-based high cycle fatigue testing," *Strain Anal. Eng. Des.*, Feb. 2022, doi: 10.1177/03093247221076765.

[12] O. Scott-Emuakpor, T. George, C. Holycross, and C. Cross, “Improved Hybrid Specimen for Vibration Bending Fatigue,” in *Fracture, Fatigue, Failure and Damage Evolution, Volume 8*, A. T. Zehnder, J. Carroll, K. Hazeli, R. B. Berke, G. Pataky, M. Cavalli, A. M. Beese, and S. Xia, Eds., in Conference Proceedings of the Society for Experimental Mechanics Series. Cham: Springer International Publishing, 2017, pp. 21–30. doi: 10.1007/978-3-319-42195-7_4.

[13] O. Scott-Emuakpor, J. Schwartz, T. George, C. Holycross, C. Cross, and J. Slater, “Bending fatigue life characterisation of direct metal laser sintering nickel alloy 718,” *Fatigue Fract. Eng. Mater. Struct.*, vol. 38, no. 9, pp. 1105–1117, 2015, doi: 10.1111/ffe.12286.

[14] J. Carr, J. Baqersad, C. Niezrecki, P. Avitabile, and M. Slattery, “Dynamic Stress–Strain on Turbine Blade Using Digital Image Correlation Techniques Part 1: Static Load and Calibration,” in *Experimental Dynamics Substructuring and Wind Turbine Dynamics*, Springer, Feb. 2012, pp. 215–220. doi: 10.1007/978-1-4614-2422-2_20.

[15] P. Reu, “Introduction to Digital Image Correlation: Best Practices and Applications,” *Exp. Tech.*, vol. 36, no. 1, pp. 3–4, 2012, doi: 10.1111/j.1747-1567.2011.00798.x.

[16] P. Reu, “All about Speckles: Contrast,” *Exp. Tech.*, vol. 39, no. 1, pp. 1–2, 2015, doi: 10.1111/ext.12126.

[17] P. Reu, “Stereo-Rig Design: Creating the Stereo-Rig Layout – Part 1,” *Exp. Tech.*, vol. 36, no. 5, pp. 3–4, 2012, doi: 10.1111/j.1747-1567.2012.00871.x.

[18] E. Jones *et al.*, “A Good Practices Guide for Digital Image Correlation,” International Digital Image Correlation Society, Oct. 2018. doi: 10.32720/idics/gpg.ed1/print.format.

[19] H. Schreier, J.-J. Orteu, and M. A. Sutton, *Image Correlation for Shape, Motion and Deformation Measurements: Basic Concepts,Theory and Applications*. Boston, MA: Springer US, 2009. doi: 10.1007/978-0-387-78747-3.

[20] T. Q. Thai, R. J. Rowley, R. S. Hansen, and R. B. Berke, “How light emitted at high temperature affects common digital image correlation algorithms,” *Meas. Sci. Technol.*, vol. 32, no. 12, p. 129401, Oct. 2021, doi: 10.1088/1361-6501/ac2319.

[21] S. R. Jarrett, “The Effect of Bit Depth on High Temperature Digital Image Correlation Measurements,” Research Thesis, Utah State University, Logan, 2021. [Online]. Available: https://digitalcommons.usu.edu/cgi/viewcontent.cgi?article=9439&context=etd

[22] W. D. Craig, F. B. Van Leeuwen, S. R. Jarrett, R. S. Hansen, and R. B. Berke, "Using text as a native speckle pattern in digital image correlation," *J. Strain Anal. Eng. Des.*, vol. 57, no. 7, pp. 539–555, Oct. 2022, doi: 10.1177/03093247211045602.

[23] P. Reu, "Stereo-rig Design: Lighting—Part 5," *Exp. Tech.*, vol. 37, no. 3, pp. 1–2, 2013, doi: 10.1111/ext.12020.

[24] T. Q. Thai, R. S. Hansen, A. J. Smith, J. Lambros, and R. B. Berke, "Importance of Exposure Time on DIC Measurement Uncertainty at Extreme Temperatures," *Exp. Tech.*, vol. 43, no. 3, pp. 261–271, Jun. 2019, doi: 10.1007/s40799-019-00313-3.

[25] S. R. Jarrett, T. Q. Thai, L. J. Rowley, W. D. Craig, and R. B. Berke, "The Effect of Bit Depth on High-Temperature Digital Image Correlation Measurements," *J. Sens.*, vol. 2022, pp. 1–19, Jun. 2022, doi: 10.1155/2022/6554128.

[26] T. Thai, "Improvement of Ultraviolet Digital Image Correlation (UV-DIC) at Extreme Temperatures," Research Thesis, Utah State University, Logan, 2020. [Online]. Available: https://digitalcommons.usu.edu/etd/7770

[27] T. Thai, "Importance of Exposure Time on Digital Image Correlation (DIC) at Extreme Temperatures," Utah State University, 2018. [Online]. Available: https://digitalcommons.usu.edu/etd/7067

[28] R. B. Berke and J. Lambros, "Ultraviolet digital image correlation (UV-DIC) for high temperature applications," *Rev. Sci. Instrum.*, vol. 85, no. 4, p. 045121, Apr. 2014, doi: 10.1063/1.4871991.

[29] T. Archer, P. Beauchêne, C. Huchette, and F. Hild, "Global digital image correlation up to very high temperatures with grey level corrections," *Meas. Sci. Technol.*, vol. 31, no. 2, p. 024003, Nov. 2019, doi: 10.1088/1361-6501/ab461e.

[30] B. Furman, B. Hill, J. Rigby, and R. Berke, "Sensor Synchronized DIC: A Robust Approach to Camera-Based Modal Analysis Using Low Framerate Cameras," *J. Sound Vib*, In review.

[31] P. Meyer and A. M. Waas, "Measurement of In Situ-Full-Field Strain Maps on Ceramic Matrix Composites at Elevated Temperature Using Digital Image Correlation," *Exp. Mech.*, vol. 55, no. 5, pp. 795–802, Jun. 2015, doi: 10.1007/s11340-014-9979-7.

[32] R. S. Hansen, K. Z. Burn, C. M. Rigby, E. K. Ashby, E. K. Nickerson, and R. B. Berke, "Digital image correlation at long working distances: The influence of diffraction limits," *Measurement*, vol. 189, p. 110493, Feb. 2022, doi: 10.1016/j.measurement.2021.110493.

[33] P. Reu, "Stereo-rig Design: Lens Selection – Part 3," *Exp. Tech.*, vol. 37, no. 1, pp. 1–3, 2013, doi: 10.1111/ext.12000.

[34] P. Reu, “Calibration: A good calibration image,” *Exp. Tech.*, vol. 37, no. 6, pp. 1–3, 2013, doi: 10.1111/ext.12059.

[35] E. Zappa, P. Mazzoleni, and A. Matinmanesh, “Uncertainty assessment of digital image correlation method in dynamic applications,” *Opt. Lasers Eng.*, vol. 56, pp. 140–151, May 2014, doi: 10.1016/j.optlaseng.2013.12.016.

[36] “Prosilica GT Technical Manual,” Allied Vision Technology, V3.2.1, Jul. 2023.

[37] E. M. C. Jones and P. L. Reu, “Distortion of Digital Image Correlation (DIC) Displacements and Strains from Heat Waves,” *Exp. Mech.*, vol. 58, no. 7, pp. 1133–1156, Sep. 2018, doi: 10.1007/s11340-017-0354-3.

[38] M. D. Novak and F. W. Zok, “High-temperature materials testing with full-field strain measurement: Experimental design and practice,” *Rev. Sci. Instrum.*, vol. 82, no. 11, p. 115101, Nov. 2011, doi: 10.1063/1.3657835.

[39] B. Pan, D. Wu, Z. Wang, and Y. Xia, “High-temperature digital image correlation method for full-field deformation measurement at 1200 °C,” *Meas. Sci. Technol.*, vol. 22, no. 1, p. 015701, Nov. 2010, doi: 10.1088/0957-0233/22/1/015701.

[40] J. Blaber, B. S. Adair, and A. Antoniou, “A methodology for high resolution digital image correlation in high temperature experiments,” *Rev. Sci. Instrum.*, vol. 86, no. 3, p. 035111, Mar. 2015, doi: 10.1063/1.4915345.

[41] T. Q. Thai, A. J. Smith, R. J. Rowley, P. R. Gradl, and R. B. Berke, “Change of exposure time mid-test in high temperature DIC measurement,” *Meas. Sci. Technol.*, vol. 31, no. 7, p. 075402, Apr. 2020, doi: 10.1088/1361-6501/ab7bbf.

[42] “What are response surface designs, central composite designs, and Box-Behnken designs?” Accessed: Aug. 01, 2023. [Online]. Available: https://support.minitab.com/en-us/minitab/21/help-and-how-to/statistical-modeling/doe/supporting-topics/response-surface-designs/response-surface-central-composite-and-box-behnken-designs/#what-is-a-central-composite-design

[43] P. Bevington and D. Robinson, *Data Reduction and Error Analysis for the Physical Sciences*. McGraw-Hill Education, 2003.

[44] B. Furman, “Development of a High-Throughput Methodology for Vibration-Based Fatigue Tests,” Utah State University, Logan, UT, 2024.

[45] “Measuring Strain with Strain Gages.” Accessed: Apr. 10, 2024. [Online]. Available: https://www.ni.com/en/shop/data-acquisition/sensor-fundamentals/measuring-strain-with-strain-gages.html

[46] “Operating Instructions: Vibrometer Controller (OFV-5000),” Polytec, Germany, User Manual 41152-Man-Vib-OFV5000-3G-0917–14en, 2014.

APPENDIX

APPENDIX A

UNCERTAINTY ANALYSIS WITH STRAIN GAGE

To determine the uncertainty in the results depicted in Figure 20, the Monte-Carlo Method (MCM) of uncertainty propagation was used. The data reduction equation being examined in this work is the absolute percent relative error equation described in Eq. 4.1. From equation 4.1, it is evident that the uncertainties in calculating the strain from the displacement measurement and from the Euler-Bernoulli solution must first be quantified. Figure 25 depicts a flowchart of the strategy of determining the uncertainty in the percent relative error measurements.

Figure 25

Flowchart for Uncertainty Analysis of Percent Relative Error Equation

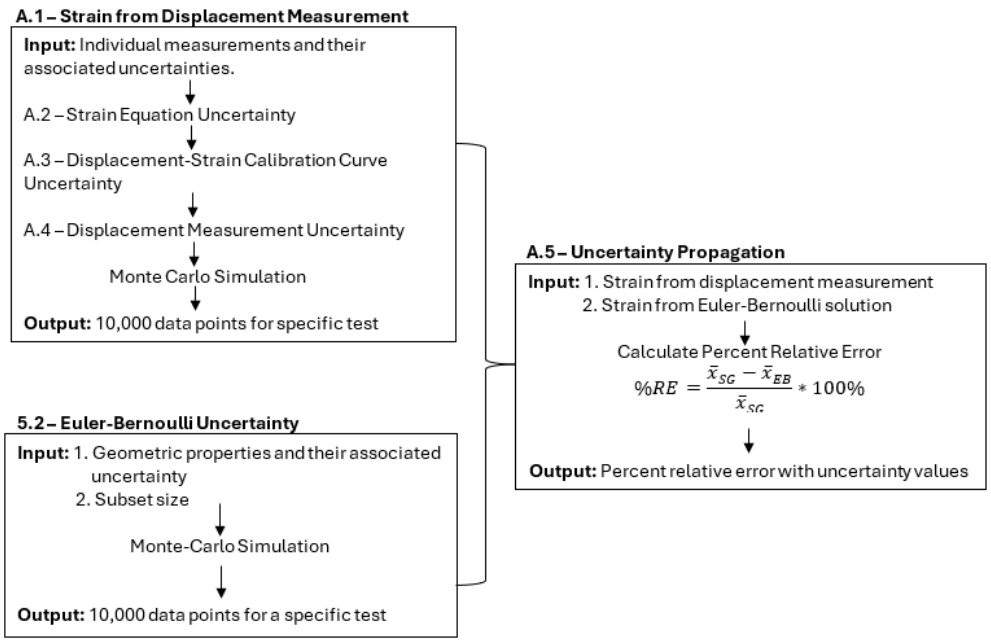

A.1 Strain from Displacement Measurement

The goal of this section is to determine the uncertainty in the strain measurement that was calculated using the strain-displacement calibration curve and the displacement reading of the laser vibrometer. The strain-displacement calibration curve takes the general form

$$\epsilon = a + bx \tag{A.1}$$

where a and b are coefficients of the linear fit and x is the displacement as measured by the laser vibrometer. To determine the uncertainty in the strain measurement, the uncertainty from the strain gage equation, uncertainty from linear fit parameters, and the uncertainty in the displacement reading from the laser vibrometer must first be determined.

A.2 Strain Equation Uncertainty Estimation

For a quarter bridge configuration, the strain gage converts voltage into strain using the following equation [45]

$$\epsilon_{xx} = \frac{4V_0}{V_{ex}G_f G_{amp}\left(1 + 2\left(\frac{V_0}{V_{ex}G_{amp}}\right)\right)} \tag{A.2}$$

where V_o is the output of the voltage of the quarter bridge circuit, V_{ex} is the excitation voltage applied to the Wheatstone Bridge, G_f is the gage factor of the strain gage, and G_{amp} is the gain supplied by the amplifier. Since $V_{ex}G_{amp}$ are much larger than V_0, the equation can be simplified and rewritten into Eq A.3 without any significant loss in accuracy.

$$\frac{\epsilon_{xx}}{V_0} = \frac{4}{G_f V_{ex} G_{amp}} \tag{A.3}$$

The uncertainty in Eq. A.3 can be determined by a straight-forward application of the Taylor-Series propagation method as shown in Eq A.4 [43]. For this particular case, since V_{ex}, G_f, and G_{amp} are measured independently, the correlation terms go to zero.

$$u_z^2 = u_x^2\left(\frac{\partial z}{\partial x}\right)^2 + u_y^2\left(\frac{\partial z}{\partial y}\right)^2 + 2u_{xy}\left(\frac{\partial z}{\partial x}\right)\left(\frac{\partial z}{\partial y}\right) \tag{A.4}$$

The uncertainty of G_f is based on the manufacturer's rated uncertainty of the strain gage (±0.5%). The combined uncertainty of $V_{ex}G_{amp}$ was determined by performing a shunt calibration and measuring the total system gain of the Wheatstone bridge (±0.25%). As such, the overall uncertainty in Eq. 8.3 was determined to be ±0.56%.

A.3 Displacement-Strain Calibration Curve Uncertainty

The uncertainty of the coefficients from the displacement-strain calibration curve can be determined using the uncertainty estimation equations by Smith and Neal for linear fit with unique uncertainties

$$u_a^2 = \frac{1}{\Delta}\sum\frac{x_i^2}{u_{y_i}^2} \tag{A.5}$$

$$u_b^2 = \frac{1}{\Delta}\sum\frac{1}{u_i^2} \tag{A.6}$$

$$\Delta = \sum\frac{1}{u_i^2}\sum\frac{x_i^2}{u_i^2} - \left(\sum\frac{x_i}{u_i}\right)^2 \tag{A.7}$$

where u_i is the uncertainty in the strain measurement. For this work, the uncertainty in the strain measurement will include the following uncertainty sources: amplitude, misalignment of strain gage, and strain equation. Table 7 summarizes the magnitude of the uncertainty sources.

Table 7

Uncertainty Sources for the Displacement-Strain Calibration Curve

Source	Uncertainty (95%)
Amplitude Read by Data Physics Controller	±0.2%
Peak Selection from test data	±0.1 $\mu\epsilon$
Misalignment of Strain Gage	±0.1%
Strain Equation	±0.56%

The uncertainties from the different sources listed in Table 7 were combined using Eq 5.2 to determine the total uncertainty for each measurement point on the displacement-strain calibration curve. Table 8 shows the resulting uncertainties in the displacement-strain calibration curve coefficients for the ring lights and strobe lights that were used in this work.

Table 8

Uncertainty in Strain-Displacement Calibration Curve Fit Parameters

Light Source	a (95% Uncertainty)	B (95% Uncertainty)
Ring Lights	1.732 ± 1.127	3.472 ± 0.0162
Strobe Lights	4.720 ± 1.8226	3.415 ± 0.018

A.4 Displacement Measurement Uncertainty

The two sources of uncertainty in the displacement measurement from the laser vibrometer considered in this work are linearity error and the random uncertainty from the

dwell feedback loop. The manufacturer specifies a linearity error of ±0.5% [46] and it is assumed that this represents a 95% confidence interval. The random uncertainty from the dwell feedback loop is unique to a specific dwell test as was explained in Chapter 4.

The uncertainty from the dwell feedback loop and the linearity error are combined using Eq. 5.2. Table 9 summarizes the mean and total uncertainty from the laser vibrometer reading for each aperture size.

Table 9

Mean Displacement and Uncertainty from Displacements Measured by Laser Vibrometer during Testing

External Light Source	Aperture Size	Mean Displacement (μm)	Uncertainty (95%)
Ring Lights	f/5.6 (wide)	619.983	±0.78%
	f/11 (moderate)	619.974	±1.09%
	f/22 (moderate/narrow)	620.266	±0.55%
Strobe Lights	f/16 (moderate)	628.690	±2.19%
	f/22 (moderate/narrow)	628.484	±1.61%
	f/32 (narrow)	628.525	±1.48%

A.5 Uncertainty Propagation

The uncertainty in the Euler-Bernoulli strain calculation was analyzed in Chapter 5. With an understanding of the uncertainty sources and magnitudes present in the displacement-strain calibration curve and the Euler-Bernoulli solution, the uncertainty can be propagated through Eq. 4.1 using the same general technique as used in Chapter 5. The Minitab contour plots of the tolerance range are shown in Figure 26. Notably, the general

shape of the contour plots presented here differ than the contour plots presented in Chapter 5. However, the same general conclusions discussed in Chapter 6 still apply.

Figure 26

Tolerance Ranges from MCM Uncertainty Analysis for Ring Lights (a) Wide, (b) Moderate, (c) Moderate/Narrow, and Strobe Lights (d) Moderate, (e) Moderate/Narrow, and (f) Narrow. Test Lighting Conditions from Table 3 and Table 4 are shown as Black Points

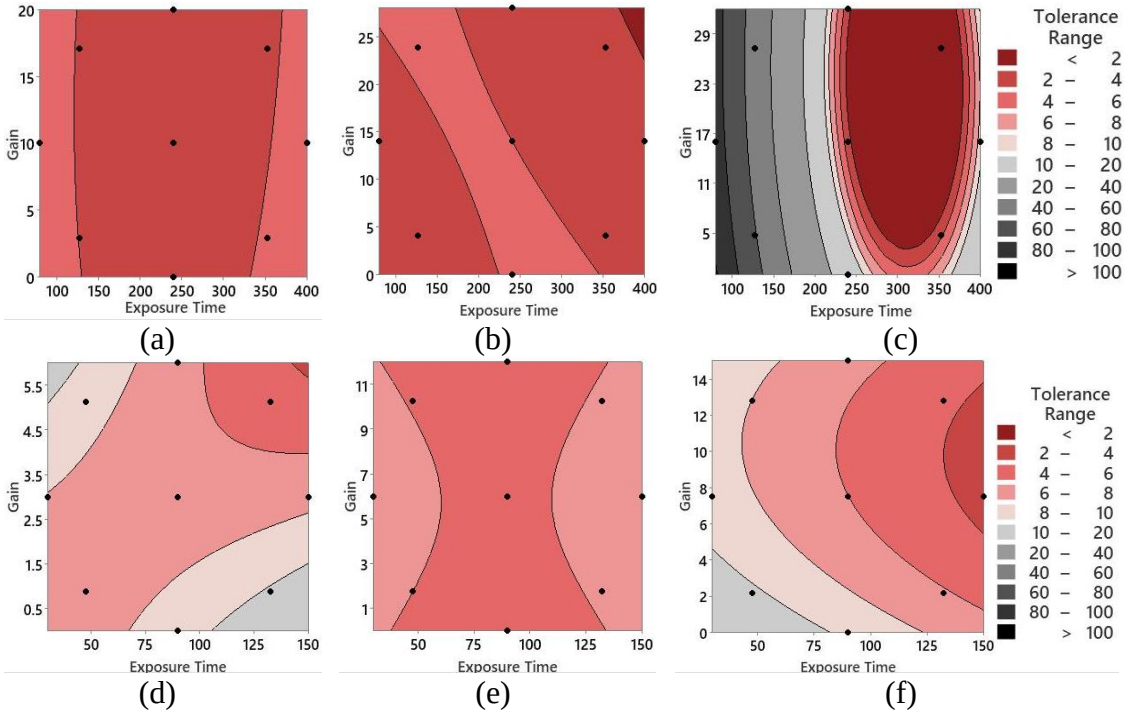

The largest source of propagated uncertainty is from the uncertainty in the displacement measurement recorded by the laser vibrometer. The exact contribution of the displacement measurement uncertainty is dependent on the aperture size but ranged from 0.27%-68.22% of the total uncertainty range. This impact is directly correlated to the spikes observed in Figure 19, which increased the uncertainty in the mean displacement, as seen in Table 9. As such, it is not surprising that the strobe light moderate aperture had an

average contribution of 58.59% of the total uncertainty be from the displacement measurement. The second largest source of uncertainty was the variation in subset size.